STRUCTURE-PROPERTY RELATIONS OF PORCINE TRABECULAR BONE AND MICRO-CT IMAGING OF VARIOUS MATERIALS

BY

WOOWON LEE

THESIS

Submitted in partial fulfillment of the requirements
for the degree of Master of Science in Mechanical Engineering
in the Graduate College of the
University of Illinois at Urbana-Champaign, 2013

Urbana, Illinois

Adviser:

Professor Iwona M. Jasiuk

Abstract

This thesis addresses the characterization of materials with a focus on trabecular bone.

In the first part, we aim to find relations between morphological measures of trabecular bone and its Young's modulus and ultimate compressive strength. Previous research has showed that apparent density and porosity are the main factors that influence mechanical properties of trabecular bone. However, due to the complex structure of trabecular bone, additional parameters may be needed to accurately predict trabecular bone's properties. Thus, we measure the apparent density, mineral content, trabecular orientation, trabecular thickness, fractal dimension, surface area and connectivity of the 6 month porcine trabecular bone using micro-computed tomography (micro-CT) and investigate how they influence Young's modulus and strength measured using uniaxial compression test. To further investigate the effect of mineral density on mechanical properties of bone, a separate experiment was conducted on bovine trabecular bone. Demineralized bovine bone samples show a dramatic decrease in mechanical properties indicating the importance of mineral density. Effects of preservation (fresh, and 1 and 5 year freeze durations) and micro-CT radiation are also investigated. Cylindrical porcine specimens were made from femoral head and divided into three groups depending on the freezing period. We conclude, using multiple regression, that porosity and apparent density are the major factors that contribute to the ultimate strength but other parameters also contribute and combined provide a more accurate prediction of bone strength. We also find that long term freezing influences mechanical properties of bone. Bones which were not frozen have higher Young's modulus and ultimate stress than the bones which were frozen for a long period of time. Also, the influence of porosity and apparent density on the mechanical properties is more dominant for

fresh bone. Furthermore, the structure-property relations for long-term frozen trabecular bone are more complex.

In the second part, various materials were scanned using a high resolution micro-CT. Micro-CT is an effective imaging modality utilized in many research areas. Taking advantage of this tool, parameters such as porosity, mineral content and perimeter were measured without destroying the materials. These materials are frog tarsus bone, thermoplastic fiber reinforced composites, and metal-carbon materials called covetics, all from collaborative projects. The mineral content of frog bones agrees well with measurements in literature. For thermoplastic composites, with randomly arranged long fibers, the fiber orientation measurements obtained using micro-CT is more accurate than using the optical imaging analysis method. Porosity of metal-carbone materials called covetics was also measured. In short, we used the micro-CT to characterize porosity and microarchitectures of biological materials such as bone, polymer matrix composites and metal-based materials.

Acknowledgments

I thank the staff at Beckman Institute ITG, Leilei Yin and Mark Bee for their help on operating micro-CT equipment, Travis Ross and Scott Robinson for their assistance in micro-CT imaging. I also thank Professor Ryan Roeder from University of Notre Dame for providing standards and his guidance on measuring mineral content. This research was supported by the National Science Foundation (CMMI 09-27909 ARRA, Dr. Ken Chong).

Table of Contents

Part 1. VARIOUS PARAMETERS CONTRIBUTING TO THE MECHANICAL PROPERTIES OF PORCINE TRABECULAR BONE

Chapter 1. Introduction

Trabecular bone (also called cancellous or spongy bone) represents roughly 20% of the bone matter in the human body [1] with the porosity ranging from 30-90%. It has a complex composite structure, consisting of collagen and other proteins, hydroxyapatite minerals and fluid-filled voids. Because of its porous structure, trabecular bone is strongly affected by age related diseases like osteoporosis. Thus, understanding of the structure-property relations of trabecular bone is critical for many biomedical applications such as assessments of treatments of osteoporosis, implants used for arthroplasty and the developments of orthoses. Due to the complexity of the trabecular bone structure the correlations between morphological descriptors and mechanical properties are still not clear. Numerous studies have been done correlating the porosity and apparent density to the mechanical properties of trabecular bone. These studies clearly show that lower porosity and higher apparent density result in stronger trabecular bone [2-8]. However, these two factors do not fully capture the mechanical properties of trabecular bone because additional morphological quantities also correlate with properties as discussed in [9-11] among others.

In this study we measure several morphological parameters of trabecular bone using micro-computed tomography (micro-CT) and investigate how they contribute to Young's modulus and ultimate compressive strength of bone which are measured by a compression test. We conduct this study using a 6 month porcine trabecular bone from femoral heads. We selected

the porcine bone due to the fact that its anatomy is similar to the one of the human bone and due to its availability. This research is motivated by the fact that multiple morphological parameters should lead to improved predictions of mechanical properties of trabecular bone. This research expands on this idea by selecting several morphological and material parameters and linking them simultaneously by multiple linear regression. Effects of freeze duration and X-ray radiation are also investigated.

High resolution micro-CT is a popular technique for imaging bone. The strengths of this method are that it is non-destructive and requires minimum sample preparation. High resolution three dimensional (3D) images provide quantitative measurements of the bone structure [12, 13]. This study is utilizing this technique by obtaining different morphological parameters on bone samples prior to testing them using the uniaxial compression test. The data obtained by the micro-CT can also serve as inputs to experimentally-based finite element models of trabecular bone.

In summary, the objective of the research discussed in this section is to find a linear equation which can predict mechanical behavior of trabecular bone using morphological and material parameters as inputs. We also investigate effects of freeze-thawing and X-ray radiation.

Chapter 2. Materials and Methods

2.1 Sample preparation

Porcine 6-month-old femurs, from species swine (*Sus scrofa domestica*), were obtained from the Meat Science Lab at the University of Illinois at Urbana-Champaign (UIUC). All pigs were healthy, raised under diets satisfying nutrient levels recommended by Nutrient Requirements of Swine (NRS, 2012). After harvesting, the femurs were either tested fresh or stored in the freezer at $-20^{o}C$ in plastic bags wrapped in a 0.1M Phosphate Buffered Saline (PBS) soaked gauze. Femurs were stored two different time lengths: one year and 5 years. Prior to preparing samples, each frozen femur was thawed for approximately 24 hours in refrigerator at $4^{o}C$. Then, the femoral head was separated from the femur by a 15-Amp band saw (RIDGID, Elyria, OH), cutting through the transverse direction. After cutting the femoral head into half, a Heavy-Duty Bench-Top Drill Press (Grizzly Industrial, Inc., Springfield, MO) and 4 mm cylindrical blade (Hager & Meisinger GmbH) were used to form cylindrical samples. All samples were cut in the longitudinal direction, excluding the exterior bone shell, as shown in Fig 1; 6-8 specimens were made from each femoral head. We used the aspect ratio 2:1 for the uniaxial compression test samples following [14]. To achieve such aspect ratio (height 8 mm x diameter 4 mm) the top and bottom surfaces of the samples were polished with a grinder (Ecomet 3000, Buehler, Lake Bluff, IL). Soft tissue was removed by using a water flosser (Wp-60W, WaterPik, Fort Collins, CO). Each sample was carefully labeled, placed in a container filed with PBS and stored in the refrigerator ($4^{o}C$) until micro-CT imaging and compression testing. All samples were imaged and tested within 48 hours from sample preparation.

2.2 Micro-CT an image post-processing

Each cylindrical trabecular bone sample was taken out of PBS filled container with tweezers and the remaining PBS was removed by placing the sample on a tissue paper. Next, the samples were fixed for micro-CT imaging by placing them in a plastic foam and mounted on a standard Xradia micro-CT sample holder. Xradia micro-CT (MicroXCT-200, Pleasanton, CA) with a 2X magnification was used to obtain the micro-CT images while rotating the sample from 0 to 190 degrees. The voltage and power for the X-ray were 40KeV and 10W, respectively, and the camera exposure time was 5 seconds. Total 381 slices were taken for approximately 90 minutes. The voxel size of the image file was approximately 10x10x10 μm^3 which is adequate for accurately imaging the trabecular architecture [15]. Standard Xradia software (XMController, XMReconstructor, XM3DViewer) was used for scanning, reconstruction and exporting image files for post-processing. The reconstruction process included alignment optimization and beam hardening correction. XM3DViewer program converted the file to an ooc file which was compatible with image post-processing software, AMIRA.

Image post-processing was completed by AMIRA software (version 5.4.2, Visage Imaging, Inc., Berlin., Germany). First, the ooc file images were translated to a 16bit grayscale (0-255) to easily separate the bone and void by the threshold. As a result of the separation, binarized label field was created. On this label field, quantitative analysis was done by the Quantification module measuring the parameters listed in Table 1.

To measure porosity, a region of interest was selected by the boundary box in the middle of the sample image. Then, the number of voxels inside the boundary box for bone and void were counted. The number of voxels was considered equal to the actual volume and used for calculating the porosity. In short, the porosity is defined as (number of void voxels)/(total

number of voxels). Euler characteristic [16], also known as Euler-Poincare number or Connectivity factor, is a characteristic of a 3D structure which is topologically invariant and measures how many connections in a structure can be severed before the structure separates into two pieces. Fractal dimension represents the roughness of an irregular structure by observing the self-similarity over different scales [17, 18]. AMIRA software used the fixed grid scan box counting method for this calculation. For orientations, AMIRA software was able to measure two orientation types. Orientation and second orientation were defined as eigenvectors of the moment of inertia matrix. The angle between the orientation, second orientation of the particle and the Z axis (longitudinal axis) was the result of the command 'OrientationPhi' in the Quantification module. The range was from 0 to 90 degrees. Fragmentation is another indicator of connectivity. It compares the volume and surface of the binarized image before and after an image dilatation. Lower fragmentation signifies better connect area while higher fragmentation means a more disconnected structure. 'AVERAGE_OBJECT_THICKNESS' command measures the thickness of the structure for a 3D image. Cylinder rod model (4/((object surface)/(object volume))) was selected to obtain the thickness of trabecular rods.

2.3 Measuring mineral content

After the initial scanning with micro-CT to obtain trabecular bone morphology, the porcine samples were scanned again to measure the average mineral volume density. High mineral density composite calibration phantoms were used to measure the hydroxyapatite volume density following [19]. There were total 7 different phantoms in the range of 0-1860 mg HA/cm^3 indicated as 0, 10, 20, 30, 40, 50, 60% by volume. Each phantom was scanned with micro-CT (MicroXCT-200, Pleasanton, CA) while immersed in PBS and maintaining same settings: the magnification (2X), voltage (40KeV), power (10W) and beam

hardening coefficient (2). Standard water phantoms (1.16 HU scale) were then scanned using the same settings and all the intensity factors from the phantoms were calibrated to the Hounsfield scale using the Xradia software. This process is called CT-scaling. As a result, a quadratic curve was created which was the HU scale versus HA volume fraction as shown in Figure 5. Cylindrical demineralized bovine bone sample were tested for verification of this method and the result was fairly close to 0 (0.36%, 2.57%). The porcine trabecular bone samples were then scanned in the same settings and, using this quadratic curve, the average mineral content of each trabecular bone sample was measured.

2.4 Deprotenization and Demineralization

Bovine femurs, 12-24 months old, were acquired from Meat Science Lab at UIUC. The methods for sample cutting and preserving were identical to those for porcine femurs mentioned in the previous section. Total of 25 cylindrical samples with an aspect ratio 2:1 were made out of 6 femoral heads.

For demineralization process (DM), samples 1 to 12 were stored in separate clearly marked containers filled with 0.6N hydrochloric acid (HCl). The solution was replaced every day for a week and was kept at room temperature. For deprotenization process (DP), samples 13 to 23 were also kept in separate marked containers filled with bleach. Similarly as for the demineralization process, the solution was replaced every day for 14 days [20]. Samples 24 and 25 where preserved in the refrigerator without any chemical treatment. These samples are called untreated (UT). After the chemical processes were complete, all samples were washed in deionized (DI) water. Then, they were stored in PBS while in refrigerator until the next experiment. During this process two samples were damaged. Thus, the remaining samples were 11 demineralized samples, 10 deproteinized samples, and two untreated samples. All samples

(UT, DM and DP) had stand-alone structures so mechanical testing could be performed afterwards. DM samples were also used to verify the validity of hydroxyapatite phantoms mentioned above.

2.5 Compression test

Before the compression test, densities of each sample were measured. First, samples were put on a tissue paper to remove the PBS from the exterior and then they were placed on a centrifuge 5415d (Eppendorf, Hauppauge, NY) with a speed of 11000rpm for 15 minutes to remove fluid from bone's interior. To prevent the samples from being damaged, they were wrapped in tissue paper while in the centrifuge and then weighted using an electrical scale. The weight (and the volume obtained from micro-CT) was used for calculating the apparent density and density [21-23].

An MTS Insight electromechanical testing system, MTS with a 2000N load cell (MTS systems Corp., Eden Prairie, MN) was used for uniaxial compression testing. All samples were kept in the refrigerator ($4^{o}C$) immersed in PBS until the experiment. Tweezers were used to pull out samples from the container and PBS inside the pores was eliminated by hand wipes. Then, each cylindrical trabecular bone sample was placed in the middle of the bottom platen and the top platen was adjusted as close as possible to the sample without any load applied. No preload was applied for the compression test and platen speed was 0.005mm/s. The test was stopped after the load passed its maximum and started decreasing. The engineering stress-engineering strain curves were obtained, with a representative one shown in Figure 6. The slope of the "linear portion" of the stress-strain curve was used to evaluate Young's Modulus [24] and the maximum stress of the stress-strain curve gave the ultimate compressive strength.

For the chemically treated bovine trabecular bone samples, the same 2kN elecro-mechanical load cell was used for the uniaxial compression testing. Beforehand, PBS was removed by wipes and then the compression test was conducted with a 0.005mm/s load cell speed. The compression test was done twice before and after demineralization or deproteinization on each sample to compare the Young's modulus before and after the chemical treatments. For the first tests (before the chemical treatments), the compression test on untreated trabecular bone samples was stopped when the load reached 100N. Considering the cross section, the maximum stress that was applied to the samples was approximately 8MPa. This was to prevent the sample from being damaged and remain in the elastic region. Then, the second test was done after demineralization and deprotenization past the maximum load.

2.6 Freeze-thawing effect

The effect of freezing was studied using 6 month porcine femurs. The studied trabecular bones were from three different harvest dates. Some bones were stored in the freezer and some were tested fresh just after harvesting. The samples were divided into the following three groups: group A (20 samples) with bones frozen for 5 years, group B (23 samples) with bones frozen for 1 year, and group C (24 samples) with bones not frozen, tested right after harvesting. Descriptions of these three groups are summarized in Table 2. Three femurs from each group were used for this study. First, normality test was done on compression test results to see if they had a normal distribution. Then, one way ANOVA test was used by OriginPro 9 (OriginLab Corporation., Northampton, MA., USA) to test the significant differences of mean and variance.

2.7 Radiation effect

Since compression test results were done after micro-CT imaging we next investigated whether micro-CT X-rays affected mechanical properties of trabecular bone. To study this

problem, a uniaxial compression test was done on separate 6 month porcine trabecular bone samples within the elastic limit. Porcine bones were cylindrical (n=5) with the aspect ratio 2:1. The resulting load-displacement curve was converted to the stress-strain curve and Young's modulus was calculated. Then, all samples were scanned with Xradia for approximately 2 hours. The setting was identical to actual experiments used on trabecular bone except for the camera exposure time (6 seconds). Lastly, the same platen compression test was conducted on the samples to measure Young's modulus. Young's modulus before and after irradiation was compared.

Chapter 3. Results

Results for Young's modulus measured before and after chemical processing (demineralization and deprotenization) are shown in Figure 7. There is a dramatic decrease in the elastic modulus of both demineralized and deproteinized samples. Young's modulus of the demineralized samples decreases on average to 0.13% of the mean elastic modulus of the untreated bone while the deproteinized samples decrease to 11.03% of the mean modulus. Thus Young's modulus of the demineralized samples drops more sharply. Young's modulus before any chemical process varies by sample and this trend remains after the chemical process. As a result, the correlation coefficient between the untreated and demineralized trabecular bone data is 0.69 and 0.68 between the untreated and deporteinized trabecular bone.

Effects of freezing on the mechanical properties, studied using porcine bone samples from three groups (Table 2), are summarized in Table 3 and Figure 8. All three groups went through the normality test for both Young's modulus and ultimate compressive strength and followed the normal distribution. One way ANOVA test and Turkey test were applied to the data with results shown in Table 3. The p value for the variance is higher than the significant level (0.05) for both Young's modulus and ultimate stress but is lower for the mean. According to the Turkey test, the mean ultimate compressive strength of group C shows a significant difference compared to the other groups.

For Young's modulus, the mean of the elastic modulus of the bone from Group C is significantly higher than from the other groups. Group A (323.47MPa) and Group B (339.93MPa) are close to each other but group C (558.93MPa) is 70% higher. By using two-sample student's t-test, the mean between group C and groups A and B is significantly different ($p<0.05$). The ultimate strength gradually increases from group A to C. The differences between group A and B

(2.53MPa) are bigger than between group B and C (1.68MPa). Groups A and B give significantly different results ($p<0.05$) according to two-sample student's t-test but group B and C do not ($p>0.05$). All statistical analysis was run on OriginPro 9.

Correlation coefficients between morphological parameters and mechanical properties are higher for fresh bone as shown in Table 4. Among the morphological factors measured for each specimen, the porosity and apparent density have biggest impact on the ultimate compressive strength. This result differs by the group. The correlation coefficient between the porosity and the ultimate compressive strength is -0.59, -0.65, -0.88 and between the apparent density and the ultimate compressive strength is 0.70, 0.65, 0.85 for groups A, B and C, respectively. All other correlation coefficients are relatively lower except for the trabecular thickness. For Young's modulus, only group C shows a high correlation with porosity, trabecular thickness, and apparent density while other groups show no correlation with any parameter.

Figure 9 demonstrates the effects of X-ray radiation. According to this data, there is no difference between Young's modulus before and after X-ray exposure (the means of Young's moduli are almost equal).

Morphological parameters that are measured for samples from three different groups (Table 2) are summarized in Table 5 and linear regression coefficients are listed in Table 6. In group C, the standard deviation is lower for porosity and apparent density compared to groups A and B. This means that the variation within group C is smaller than in the two other groups. Using all the measurements obtained by AMIRA and connecting them with the mechanical properties, linear regression coefficients were obtained for each parameter. Groups were treated individually because of the results of ANOVA test. By multiplying the linear coefficient and measured value and adding all the terms together, the equation predicting the mechanical

properties was completed. The coefficient of determination in each group is group C(0.94)>B(0.59)>A(0.54) and standard error is group A(2.48), group B(2.58), group C(1.08).

Chapter 4. Discussion

Previous studies have shown that mineral density has a strong correlation with Young's modulus and ultimate compressive strength of trabecular bone [25-27]. It has been shown as well that Young's modulus of deproteinized samples drops and this decrease is less than for demineralized samples [28]. In this project, demineralized and deproteinized bones were tested and the results comply with those reported in literature. Therefore, we confirm that mineral content should be one of the parameters in the linear equation. Also, the results show that trabecular bone is a composite material with mineral and protein being continuous (interpenetrating) phases. Interestingly, statistical analysis of the 6 month porcine trabecular bone results shows that the mineral content alone has a minor effect on the Young's modulus and ultimate stress. One possible reason is that the mineral content measured is the average value of the entire bone sample and actually varies by location. Even though the correlation of mechanical properties and measured bone mineral density is weak, the main point of this study is to combine them with other parameters. As mentioned above, by combining other parameters together the linear equation will be more accurate. Another fact that brings attention is the variation on Young's modulus. UT, DM and DP samples all experienced fluctuations within the same category. After undergoing demineralization and deproteinization, stiff samples still remain to be stiff compared to others and the same with soft samples. This represents that additional micro-structural parameters are contributing to Young's modulus and it strengthens the idea of the need to add supplementary parameters.

One way ANOVA test shows that there is a significant difference between group C and the other two groups for Young's modulus. For the ultimate strength, groups A and B have largest difference. Therefore it can be concluded that there is an actual difference between the

groups. This indicates that the longer the bones are stored in a freezer, Young's modulus and ultimate stress tend to decrease. Looking how freezing will affect the mechanical properties of trabecular bone is an important problem since bone is usually stored by freezing. Effects of freezing on mechanical properties have been studied in literature and it has been found that it does not alter properties of trabecular bone [29-32]. However, most of the previous research was conducted on the bones that were frozen within 1 year while this study looks also at a much longer period of 5 years. Another difference between the groups is how closely the mechanical properties depend on the parameters such as porosity and apparent density. According to this study, group C most likely follows the reported trend that porosity is strongly related to Young's modulus and ultimate stress, while for group A and B the correlation is lower especially for Young's modulus. This indicates that the long term freezing not only weakens bone but also makes it more challenging to predict. Thus, we find that freezing trabecular bone for over 1 year significantly affects its mechanical properties.

From the comparison of Young's modulus of trabecular bone before and after being scanned by micro-CT we conclude that X-rays from the micro-CT do not affect Young's modulus. This is consistent with a similar study on bovine cortical bone made out of femur at all four directions in a cubical shape. The settings (magnification-2X, voltage-40KeV, power-10W, exposure time-5 seconds) used on Xradia were compatible with the ones used for our tests. This conclusion is also consistent with those of previous studies that irradiation does not affect the elastic properties of bone [33, 34]. We did not study the effect of X-ray radiation on the ultimate strength of trabecular bone while other studies concluded that radiation affects the post-yield properties depending on the dose level (Gy) [35, 36]. The exact dose level from each sample has not been collected but several studies confirm that by micro-CT radiation dose is lower than 1Gy

for bone [37-39], soft tissue [40, 41] and organs [42, 43]. This is too low to affect the compressive ultimate stress based on those other studies. For that reason, although the effect of X-ray on ultimate strength was not measured in our study, we assume that those effects would also be negligible.

In this study several morphological parameters were measured simultaneously for each specimen rather than just focusing on one or two parameters. As a result, the coefficient of determination increased using the multiple regression. However it is still clear that the porosity and apparent density strongly affect the mechanical properties of trabecular bone. Trabecular thickness and connectivity also have an impact to the mechanical properties but these two parameters are strongly related to porosity. Using the fact the some morphological parameters are related to each other, the number of parameters could be reduced and roughly end up with only apparent density [11]. However, the parameters addressed in this study are not closely correlated to each other. Therefore, adding these non-correlated parameters in the linear multiple regression helped to enhance the accuracy.

By plotting the compressive ultimate stress versus bone density, the 6 month porcine trabecular bones follow the trend reported in literature [44] as shown in Figure 10. The ultimate stress is normalized by 190 MPa and the bone density is normalized by 2505.58, 2732.40, 2685.97 kg/m^3 respectively for groups A, B and C. However, Young's modulus normalized by 17GPa does not match well except for group C. This is because group C was the only set of samples that were not frozen and no detrimental effect was enforced by storage. Other studies have showed that mechanical properties are proportional to the square of apparent density [45, 46]. By using the polynomial fit, group C acceptably agrees with this trend as displayed in Figure 11. The squared coefficients of determination for ultimate stress and Young's modulus are 0.72

and 0.50, respectively. However, the groups A and B do not follow this trend. Despite the fact that morphological parameters are involved, other factors could contribute to scattering. One possible reason for scatter could be that the load was not given exactly in the direction along the trabeculae direction [47]. As indicated by micro-CT, although we attempted to cut trabecular bone samples in the direction of trabeculae based on prior more crude imaging by micro-CT, a lot of struts were off-axis and this could have caused a decrease in both the compressive strength and Young's modulus. Also, the level of moisture of samples was not perfectly controlled. Since there is a variation of strength among dry and wet specimens [48], this may have caused some discrepancy.

Since the characteristics of trabecular bone cannot be explained solely by porosity, we connected other variables such as fractal dimension and connectively and accuracy increased in all three groups. This means that the mechanical properties of trabecular bone not only depend on porosity and apparent density but also on other geometric factors.

Also, our micro-CT images provide not only morphological and composition measures but also can serve as inputs for finite element simulations of mechanical response of trabecular bone.

This study has several limitations. We use in vitro porcine femurs. Although the macrostructure and microstructure of porcine bones are known to be similar to human bones [49], bone composition of trabecular bone is quite different [50] and the results may not be comparable to human bone. Also, bone mechanical properties vary among anatomical site [51] and this study focuses only on femurs. For clinical applications, similar tests should be conducted on human bones. In addition, the mechanical test in this study was a conventional platen compression test involving side-artifacts [52], friction at the specimen-platen [53] and

systematic and random errors [54]. These factors result in a under or over estimation of mechanical properties. The initial toe region which is created by these artifacts, hinders acquiring the yield stress. Yield stress could be another studied output. Using a protocol to minimize the artifacts of the compression test [55] or applying ultrasound technique [49, 50] could address some of these issues. Future research could be done involving more mechanical parameters such as fracture toughness, yield stress, viscoelastic properties and should include more parameters describing the bone structure and composition [56, 57]. Intraspecimen variation [58, 59] should be further studied and tissue properties should be measured. Fabric tensor is another factor that has shown correlation with trabecular bone mechanical properties and could be added as an additional parameter as well [60, 61]. Also, rather than using the linear regression, a nonlinear regression could be utilized. Finally, a nanoindentation technique could be used to obtain tissue level mechanical properties of trabecular bone which would provide additional inputs. Such data would be also valuable for finite element calculations [62] of trabecular bone response to mechanical loads. Finite element simulations could provide further insights into the structure-property relations of trabecular bone.

Chapter 5. Summary

After comparing the results between bones that were frozen for different periods of time, we conclude that freezing porcine femoral trabecular bones tends to reduce Young's modulus and ultimate stress. Moreover, the influence of parameters such as porosity and apparent density, that are known to affect the mechanical properties of trabecular bone, becomes weaker when bones are frozen for a long period of time.

For estimating Young's modulus and ultimate stress of trabecular bone, using more morphological parameters, obtained using high resolution micro-CT, provides more accurate predictions than those based on mineral density alone.

Part 2. MICRO-CT MEASUREMENTS OF OTHER MATERIALS

Chapter 6. Introduction

X-ray computerized tomography is a radiographic imaging method producing 3-D digital images of a volumetric object. Micro-computerized tomography is used for smaller scale imaging of samples that are under 1cm in dimension and it can provide images at greater resolution [63]. 3-D images are reconstructed from multiple 2-D images to generate cross-sectional images. Quantitative analysis can be made and the files also provide inputs for computational modeling. Because of its versatility and well known advantage of being a non-destructive 3-D imaging technique, micro-CT is extensively used for materials characterization in numerous areas. In the medical field, CT is used to image human body while micro-CT is utilized to scan bone samples [64] and other biological tissues and structures [65-67]. In material science, micro-CT is used widely to study microstructures of various materials and composites to evaluate their morphological characteristics [68].

Beckman Imaging Technology group (ITG) at UIUC has three different kinds of micro-CT equipment. First, Skyscan 1172 has a 10 micron spatial resolution and allows to image relatively big samples, up to 4 cm x 4 cm x 4 cm. It is equipped with a 100kV X-ray source and a 10 Megapixel CCD camera. The other two scanners are MicroXCT-200 and microXCT-400. These handle smaller samples and can give down to 1 micron resolution. MicroXCT-400 has supplementary features such as a larger enclosure, longer stage travel and additional baffle inputs. By using these three types of equipment, the following materials were measured in addition to the porcine and bovine bone described in Part 1: the frog tarsus bone, fiber reinforced thermoplastic and metal-carbon material.

The first studied material is a frog tarsus bone. Frog tarsus consists of two tarsal bones. The outer bone in terms of the body is thicker and straight. The inner bone is thinner and slightly curved. The former is called calcaneum while latter is called astragalus. They are fused together at the edges with a wide gap in the middle [69]. Some researchers focused on frog bone testing for investigating the jumping locomotion [70]. However, relatively few studies have been done on frog bones compared to mammalian bones (cow, rat or mouse bones). This study was aimed to compare the frog bone structure with the rat or mouse bones. The motivation for this study was a project on bone regeneration which used frog animal model [71]. My role in this project was to scan frog tarsus bone samples and measure morphological parameters including the perimeter and mineral density.

The second studied material was a thermoplastic fiber-reinforced composite. Injection molded long-fiber-reinforced thermoplastics (LFTs) compared to the short-fiber reinforced thermoplastics have enhanced mechanical properties [72, 73]. However, producing this material usually results in a non-uniform structure through the thickness of the composite panel. Fiber orientation also varies in-plane causing strongly anisotropic mechanical properties [74]. This project was aiming to evaluate the anisotropic elastic properties of LFT composite panels. Fiber orientation distribution (FODs) was measured by two different tools, optical microscope and micro-CT. The fiber orientation tensor was determined from these measurements and was used for predicting elastic properties [75]. We participated in this project by utilizing micro-CT.

The last material was 7075 Al covetics with 0, 3, 5wt% carbon. Covetics are novel material produced by Third Millennium Metals, LLC which are made of metals infused with carbon. The purpose of this study was to examine the microstructure and composition of this new material and measure its mechanical properties. These will serve as inputs and validation of a

multi scale computational model. Various materials characterization tools were used and I took part in this study by measuring porosity of the 7075 Al covetic using the micro-CT.

Chapter 7. Materials and Methods

7.1 Frog tarsus bone

7.1.1 Porosity

Dry frog bone (Xenopus laevis) femur samples were scanned using Skyscan 1172 (Aartselaar, Belgium). Because the height of the samples was relatively tall (2cm), Skyscan was preferred to Xradia micro-CT. Aluminum filter was used to generate high contrast images with the background. Voltage and current were set to 60kV and 160μA , respectively. While Skyscan was operating, the sample was rotated for one full rotation at a rotation step of 0.7 degrees. The operating time was approximately 20 minutes and all the settings were adjusted by the Control software. After imaging was complete, Nrecon software initialized the reconstruction process. During reconstruction, beam hardening correction, alignment optimization and ring artifact reduction was run. Lastly, image post processing was conducted by CTan. CTan is an image processing software which has similar functions as AMIRA software such as setting the threshold to binary images and measuring morphological parameters. To measure the porosity, an adequate threshold was selected by comparing with the original image. Based on the binarized images, porosity was calculated. A 3-D image generated by CTan is illustrated on Figure 13.

7.1.2 Perimeter and mineral content

The middle section of frog tarsus bone was scanned again by Xradia micro-CT (MicroXCT-200) to measure the perimeter and the mineral volume content. This imaging process was similar to imaging porcine bone mentioned in the previous section. The frog bone sample was fixed vertically on a plastic foam and mounted on a standard Xradia micro-CT sample holder. Magnification used was 2X and the rotating angle was 0 to 190 degrees. Since it

was unnecessary to image the whole tarsus bone, the camera was focused only on the middle section. The voltage and power for the X-ray were 40KeV, 10W and the camera exposure time was 5 seconds. Total 381 slices were taken for approximately 90 minutes. The spatial resolution of the image file was close to 11μm . Standard Xradia software (XMController, XMReconstructor, XM3DViewer) was used for scanning, reconstruction and exporting image files for post-processing. The reconstruction process included alignment optimization and beam hardening correction. XM3DViewer program converted the file to an ooc file which was compatible with AMIRA software. Figure 14 is the 3D images obtained by AMIRA software.

According to the images from micro-CT, the inner portion of frog tarsus middle section was hollow with bone forming an outer layer. The objective was to measure the perimeters of the exterior surface of bone and to do so, each portion (marked in different color) had to be counted as a different section. By only using threshold to separate bone and void, the sections could not perfectly be separated. This was because some images slice contained regions where sections were connected to each other. Therefore, the slices that contained connected parts were found and separated manually by using the brush tool. To check whether the sections were separated, I_analyze command on Quantification module was used. This command analyzes predefined parameters such as volume, length and diameter by sections and each section is represented in different colors. So manually erasing connected regions had to continue until all sections had different colors as Figure 15(c).

The original image consisted of 500 slices in the vertical direction and applying commands in Quantification gave values that included all 500 images summed together. We were interested on the perimeters on each slice not the perimeters added all together. To solve this issue, Seqfrom3D command was used to convert 3D images to a sequence image. Sequence

images could be distinguished by I_analyzeseq command and produced a table showing the parameters on each slice. However, the perimeter command on Quantification was represented in pixels on the perimeter. It is useful to know the actual length not the number of pixels. To correct this, from the label field a LineSet data which could store independent line segments was created. The next step was to convert them to Spatial Graph data. This type of data could store curved lines in 3D spaces. By showing the spatial graph statistics, a table is produced indicating the length of the lines, in this case perimeter. The flaw of this method is that the results show only one selected slice at a time. So we decided to measure the perimeter every 25 slices from 0 to 500.

For measuring the HA volume density in the frog tarsus middle section, the technique mentioned in the previous section, using composite phantoms, was applied. The equivalent setting with the phantoms was used and by Xradia standardized software, the mineral content was calculated. The middle section was divided into three sections (top, middle, bottom) and mineral content was measured on each section.

7.2 Thermoplastic composite

Fibers within the thermoplastic composite were roughly 1mm long and 17μm in diameter. Thus the resolution had to be high enough to clearly image the fibers. In this case, Xradia was preferable over Skyscan and the spatial resolution used was 4μm. The cross section of the sample (2.55 mm x 2.68 mm) was smaller than of the other samples used before so 4X magnification was applied. The setting was similar as for previous samples and scanning took around 150 minutes.

Micro-CT images could clearly capture fibers in the thermoplastic and are illustrated in Figure 16. By threshold, fibers were distinguished solely and are shown on Figure 16. (b). Since

fibers were tangled with each other, AMIRA could not analyze them individually. So the initial task was to separate them without creating a major distortion. To form a gap between weakly connected fibers, Distance map module was used for the binarized image. This module computes a 3D distance field of a 3D object. Then, after shifting the gray level by adding 10, finally much more fibers were separated. The last step was to use Quantification Orientation command which obtains the orientation of each fiber between the vertical axis. Computing the entire image (668 slices) at once took too much memory of the computer so the image was divided into 20 portions and each part had 3 slices.

7.3 Covetics

Three types of 7075 aluminum covetic samples were cut by the machine shop at Mechanical Engineering Laboratory, UIUC. These were 0%, 3% and 5% wt carbon covetics. Sample cross sections were 1? .5mm and 1-2cms in the vertical direction. MicroXCT-200 was used to measure porosity of the samples. Since covetics were not biological material like bone, a high X-ray intensity was required for high contrast images. So the voltage and power were 100keV and 10W, respectively. For high resolution, 10X lens was used and beam hardening coefficient was 5. Scanning process took around 150 minutes and post processing was completed using AMIRA software. By using the threshold, voids were distinguished from the covetic sample and 3D images of the voids are shown on Figure 20. From the binarized image, a boundary box was formed counting the number of voxels that belong to void and Al. This information provides porosity of each sample.

Chapter 8. Results

Frog tarsus bone porosity is 73.2% according to the data**.** Table 7 is illustrating the perimeters of the middle section of frog tarsus. As expected, the center part has the smallest perimeter and the top and bottom part have the biggest. The result applies to both Astragalus and Calcaneum. The difference between the largest and smallest diameters is around 2000μm on both sides. When comparing the pixels and actual length, the correlation coefficient between them is 0.99 for both bones. However, there are some points where the number of pixels are increasing whereas the actual length is decreasing. Mineral density on frog tarsus is displayed in Table 8. The top and bottom parts of the bone have less mineral than the middle section, according to the measurements. However this difference is less than 10% of the mineral density from the middle part.

Table 9 is showing orientation of the fibers on the noted slices for the thermoplastic composite. Considering the standard deviation, there is a lot of fluctuation between the fibers and most of the averages are less than 45 degrees. This means that most of the fibers are along the vertical direction or close to the vertical axis.

The porosity for each covetic sample is 0.4%, 1.7% and 1.6%. 3-D images of the pores are shown on Figure 20. For the 0% wt C covetics, there are hardly any pores. 3% and 5% covetic samples have pores evenly distributed throughout the samples. Although the porosity of the 3% and 5% covetics is similar, the void figures look different. As shown on Figure 20, 3% covetics voids are round and big while 5% covetics voids are irregular and relatively small. Each sample has its own cross section color and this is shown on Figure 19. 0% covetics has a light color while 3% has the dark color.

Chapter 9. Discussion

The mineral content complies well with the results reported in literature [76]. However, for the porosity and perimeter, there are no previous data to compare with. This is because there are relatively few studies investigating frog bone compared to those from other animals. Especially for the perimeter, it depends on the species [77] so there are difficulties finding comparable data. The reason for the porosity of frog tarsus being as high as regular trabecular bone is that the measurements included the inner hollow part of the tarsus.

On the thermoplastic project, the data measured by the micro-CT and optical microscopes were used for predicting elastic properties. Later they were compared with the experimental data. The result is that micro-CT gives a lower error than optical image analysis methods. This result shows that micro-CT is an effective tool in measuring fiber orientations of thermoplastic composite. The information about fiber orientation was then used to predict elastic properties of these compositess. Fiber orientation is a critical factor for modeling failure using finite element simulations. This is because failure strains and energy dissipation also depend on the orientation of fibers. Thus, micro-CT has been used to measure fiber orientation for fiber reinforced polymer [78] and composites [79] and the results were considerably accurate. This research is showing another example how beneficial the micro-CT is.

Carbon can be detected by micro-CT [80] so it could be possible to assume that instead of voids, carbon was detected and counted as voids. However, the porosity of 3% and 5% wt carbon covetics are 1.7% and 1.6% which are similar. Therefore, most likely these are measurements of void volume fraction. For the mechanical tests, 7075 Al covetics did show differences compared to 7075 Al alloy. To be specific, the ultimate tensile strength and yield strength increased due to carbon addition. Also, Rockwell, Vickers and nanoindentation hardness increased with the

increase in carbon content. These facts can conclude covetics actually do enhance the mechanical properties compared to base metal.

While separating fibers in the thermoplastic, a large number of them were lost. This problem could be solved by increasing the special resolution. Currently Beckman ITG has Xradia Nano-CT which produces images at resolution up to 50nms. By preparing adequate samples for Nano-CT, this could provide more accurate data. For covetics, since the size of the sample was small, the porosity calculated could contain large errors. So the next task would be to use smaller samples and image them with higher resolution. For future studies, finite element analysis could be implemented by using the micro-CT images and measurements as inputs.

Chapter 10. Summary

Micro-CT is a valuable tool used in multiple research areas. This study scanned three different materials which are frog tarsus, thermoplastic and covetics. Different kinds of measurements were analyzed after scanning and all cases took advantage of the benefits of micro-CT successfully yielding reasonable values.

References

1. Clarke, B., *Normal bone anatomy and physiology.* Clin J Am Soc Nephrol, 2008. 3 Suppl 3: p. S131-9.
2. Keaveny, T.M. and W.C. Hayes, *A 20-year perspective on the mechanical properties of trabecular bone.* J Biomech Eng, 1993. 115(4B): p. 534-42.
3. Pothuaud, L., et al., *Combination of topological parameters and bone volume fraction better predicts the mechanical properties of trabecular bone.* J Biomech, 2002. 35(8): p. 1091-9.
4. Bevill, G., et al., *Influence of bone volume fraction and architecture on computed large-deformation failure mechanisms in human trabecular bone.* Bone, 2006. 39(6): p. 1218-25.
5. Hernandez, C.J., et al., *The influence of bone volume fraction and ash fraction on bone strength and modulus.* Bone, 2001. 29(1): p. 74-8.
6. Gibson, L.J., *The mechanical behaviour of cancellous bone.* J Biomech, 1985. 18(5): p. 317-28.
7. Sanyal, A., et al., *Shear strength behavior of human trabecular bone.* J Biomech, 2012. 45(15): p. 2513-9.
8. Kopperdahl, D.L. and T.M. Keaveny, *Yield strain behavior of trabecular bone.* J Biomech, 1998. 31(7): p. 601-8.
9. Hodgskinson, R. and J.D. Currey, *The effect of variation in structure on the Young's modulus of cancellous bone: a comparison of human and non-human material.* Proc Inst Mech Eng H, 1990. 204(2): p. 115-21.
10. Hodgskinson, R. and J.D. Currey, *Effects of structural variation on Young's modulus of non-human cancellous bone.* Proc Inst Mech Eng H, 1990. 204(1): p. 43-52.
11. Goulet, R.W., et al., *The relationship between the structural and orthogonal compressive properties of trabecular bone.* J Biomech, 1994. 27(4): p. 375-89.
12. Muller, R., *Hierarchical microimaging of bone structure and function.* Nat Rev Rheumatol, 2009. 5(7): p. 373-81.
13. Burghardt, A.J., T.M. Link, and S. Majumdar, *High-resolution computed tomography for clinical imaging of bone microarchitecture.* Clin Orthop Relat Res, 2011. 469(8): p. 2179-93.
14. Keaveny, T.M., et al., *Trabecular bone modulus and strength can depend on specimen geometry.* J Biomech, 1993. 26(8): p. 991-1000.
15. Peyrin, F., et al., *Micro-CT examinations of trabecular bone samples at different resolutions: 14, 7 and 2 micron level.* Technol Health Care, 1998. 6(5-6): p. 391-401.
16. Gundersen, H.J., et al., *The Conneulor: unbiased estimation of connectivity using physical disectors under projection.* Bone, 1993. 14(3): p. 217-22.
17. Alberich-Bayarri, A., et al., *Assessment of 2D and 3D fractal dimension measurements of trabecular bone from high-spatial resolution magnetic resonance images at 3 T.* Med Phys, 2010. 37(9): p. 4930-7.
18. Mandelbrot, B.B., *The fractal geometry of nature*1982, San Francisco: W.H. Freeman. 460 p., 1 leaf of plates.
19. Deuerling, J.M., et al., *Improved accuracy of cortical bone mineralization measured by polychromatic microcomputed tomography using a novel high mineral density composite calibration phantom.* Med Phys, 2010. 37(9): p. 5138-45.

20. Hamed, E., et al., *Elastic moduli of untreated, demineralized and deproteinized cortical bone: validation of a theoretical model of bone as an interpenetrating composite material.* Acta Biomater, 2012. 8(3): p. 1080-92.

21. Carter, D.R. and W.C. Hayes, *The compressive behavior of bone as a two-phase porous structure.* J Bone Joint Surg Am, 1977. 59(7): p. 954-62.

22. Galante, J., W. Rostoker, and R.D. Ray, *Physical properties of trabecular bone.* Calcif Tissue Res, 1970. 5(3): p. 236-46.

23. Zioupos, P., R.B. Cook, and J.R. Hutchinson, *Some basic relationships between density values in cancellous and cortical bone.* J Biomech, 2008. 41(9): p. 1961-8.

24. Morgan, E.F., et al., *Nonlinear behavior of trabecular bone at small strains.* J Biomech Eng, 2001. 123(1): p. 1-9.

25. Novitskaya, E., et al., *Anisotropy in the compressive mechanical properties of bovine cortical bone and the mineral and protein constituents.* Acta Biomater, 2011. 7(8): p. 3170-7.

26. Haba, Y., et al., *bone mineral densities and mechanical properties of retrieved femoral bone samples in relation to bone mineral densities measured in the respective patients.* ScientificWorldJournal, 2012. 2012: p. 242403.

27. Houde, J., et al., *Correlation of bone mineral density and femoral neck hardness in bovine and human samples.* Calcif Tissue Int, 1995. 57(3): p. 201-5.

28. Krischak, G.D., et al., *Predictive value of bone mineral density and Singh index for the in vitro mechanical properties of cancellous bone in the femoral head.* Clin Biomech (Bristol, Avon), 1999. 14(5): p. 346-51.

29. Panjabi, M.M., et al., *Biomechanical time-tolerance of fresh cadaveric human spine specimens.* J Orthop Res, 1985. 3(3): p. 292-300.

30. Linde, F. and H.C. Sorensen, *The effect of different storage methods on the mechanical properties of trabecular bone.* J Biomech, 1993. 26(10): p. 1249-52.

31. Kang, Q., Y.H. An, and R.J. Friedman, *Effects of multiple freezing-thawing cycles on ultimate indentation load and stiffness of bovine cancellous bone.* Am J Vet Res, 1997. 58(10): p. 1171-3.

32. Borchers, R.E., et al., *Effects of selected thermal variables on the mechanical properties of trabecular bone.* Biomaterials, 1995. 16(7): p. 545-51.

33. Singhal, A., et al., *Effect of high-energy X-ray doses on bone elastic properties and residual strains.* J Mech Behav Biomed Mater, 2011. 4(8): p. 1774-86.

34. Currey, J.D., et al., *Effects of ionizing radiation on the mechanical properties of human bone.* J Orthop Res, 1997. 15(1): p. 111-7.

35. Barth, H.D., et al., *Characterization of the effects of x-ray irradiation on the hierarchical structure and mechanical properties of human cortical bone.* Biomaterials, 2011. 32(34): p. 8892-904.

36. Barth, H.D., et al., *On the effect of X-ray irradiation on the deformation and fracture behavior of human cortical bone.* Bone, 2010. 46(6): p. 1475-85.

37. Badea, C.T., et al., *In vivo small-animal imaging using micro-CT and digital subtraction angiography.* Physics in Medicine and Biology, 2008. 53(19): p. R319-R350.

38. Cao, X., et al., *Irradiation induces bone injury by damaging bone marrow microenvironment for stem cells.* Proc Natl Acad Sci U S A, 2011. 108(4): p. 1609-14.

39. Taschereau, R., P.L. Chow, and A.F. Chatziioannou, *Monte carlo simulations of dose from microCT imaging procedures in a realistic mouse phantom.* Med Phys, 2006. 33(1): p. 216-24.

40. Paulus, M.J., et al., *High resolution X-ray computed tomography: an emerging tool for small animal cancer research.* Neoplasia, 2000. 2(1-2): p. 62-70.

41. Figueroa, S.D., et al., *TLD assessment of mouse dosimetry during microCT imaging.* Med Phys, 2008. 35(9): p. 3866-74.

42. Carlson, S.K., et al., *Small animal absorbed radiation dose from serial micro-computed tomography imaging.* Mol Imaging Biol, 2007. 9(2): p. 78-82.

43. Detombe, S.A., et al., *X-ray dose delivered during a longitudinal micro-CT study has no adverse effect on cardiac and pulmonary tissue in C57BL/6 mice.* Acta Radiol, 2013.

44. Gibson, L.J. and M.F. Ashby, *Cellular solids : structure and properties*. 2nd ed. Cambridge solid state science series1997, Cambridge ; New York: Cambridge University Press. xviii, 510 p.

45. Browner, B.D. and N.E. Green, *Skeletal trauma*, in *Expert consult Premium edition*2008, Saunders,: Edinburgh. p. 1 online resource.

46. Winkelstein, B.A., *Orthopaedic biomechanics*2013, Boca Raton: Taylor & Francis. p.

47. Liu, X.S., et al., *Complete volumetric decomposition of individual trabecular plates and rods and its morphological correlations with anisotropic elastic moduli in human trabecular bone.* J Bone Miner Res, 2008. 23(2): p. 223-35.

48. Wolfram, U., H.J. Wilke, and P.K. Zysset, *Rehydration of vertebral trabecular bone: influences on its anisotropy, its stiffness and the indentation work with a view to age, gender and vertebral level.* Bone, 2010. 46(2): p. 348-54.

49. Pearce, A.I., et al., *Animal models for implant biomaterial research in bone: a review.* Eur Cell Mater, 2007. 13: p. 1-10.

50. Aerssens, J., et al., *Interspecies differences in bone composition, density, and quality: potential implications for in vivo bone research.* Endocrinology, 1998. 139(2): p. 663-70.

51. Morgan, E.F., H.H. Bayraktar, and T.M. Keaveny, *Trabecular bone modulus-density relationships depend on anatomic site.* J Biomech, 2003. 36(7): p. 897-904.

52. Bevill, G., S.K. Easley, and T.M. Keaveny, *Side-artifact errors in yield strength and elastic modulus for human trabecular bone and their dependence on bone volume fraction and anatomic site.* J Biomech, 2007. 40(15): p. 3381-8.

53. Keaveny, T.M., et al., *Theoretical analysis of the experimental artifact in trabecular bone compressive modulus.* J Biomech, 1993. 26(4-5): p. 599-607.

54. Keaveny, T.M., et al., *Systematic and random errors in compression testing of trabecular bone.* J Orthop Res, 1997. 15(1): p. 101-10.

55. Keaveny, T.M., et al., *Trabecular bone exhibits fully linear elastic behavior and yields at low strains.* J Biomech, 1994. 27(9): p. 1127-36.

56. Easley, S.K., et al., *Biomechanical effects of simulated resorption cavities in cancellous bone across a wide range of bone volume fractions.* J Bone Miner Res, 2012. 27(9): p. 1927-35.

57. Fields, A.J., et al., *Influence of vertical trabeculae on the compressive strength of the human vertebra.* J Bone Miner Res, 2011. 26(2): p. 263-9.

58. Jaasma, M.J., et al., *Biomechanical effects of intraspecimen variations in tissue modulus for trabecular bone.* J Biomech, 2002. 35(2): p. 237-46.

59. Keaveny, T.M., et al., *Biomechanics of trabecular bone.* Annu Rev Biomed Eng, 2001. 3: p. 307-33.

60. Cowin, S.C., *The relationship between the elasticity tensor and the fabric tensor.* Mechanics of Materials, 1985. 4(2): p. 137-147.

61. Haiat, G., et al., *Relationship between ultrasonic parameters and apparent trabecular bone elastic modulus: a numerical approach.* J Biomech, 2009. 42(13): p. 2033-9.

62. Keaveny, T.M., *Biomechanical computed tomography-noninvasive bone strength analysis using clinical computed tomography scans.* Ann N Y Acad Sci, 2010. 1192: p. 57-65.

63. Griffin, L.D., et al., *Improved segmentation of meteorite micro-CT images using local histograms.* Computers & Geosciences, 2012. 39(0): p. 129-134.

64. Buie, H.R., et al., *Micro-CT evaluation of bone defects: Applications to osteolytic bone metastases, bone cysts, and fracture.* Med Eng Phys, 2013.

65. de Crespigny, A., et al., *3D micro-CT imaging of the postmortem brain.* J Neurosci Methods, 2008. 171(2): p. 207-13.

66. Laperre, K., et al., *Development of micro-CT protocols for in vivo follow-up of mouse bone architecture without major radiation side effects.* Bone, 2011. 49(4): p. 613-22.

67. Metscher, B.D., *MicroCT for comparative morphology: simple staining methods allow high-contrast 3D imaging of diverse non-mineralized animal tissues.* BMC Physiol, 2009. 9: p. 11.

68. Zhang, Q., et al., *Micro-CT characterization of structural features and deformation behavior of fly ash/aluminum syntactic foam.* Acta Materialia, 2009. 57(10): p. 3003-3011.

69. Kotpal, R.L., *Modern Text Book of Zoology Vertrbrates*2010.

70. Wilson, M.P., et al., *Mechanical properties of the hindlimb bones of bullfrogs and cane toads in bending and torsion.* Anat Rec (Hoboken), 2009. 292(7): p. 935-44.

71. Song, F., B. Li, and D.L. Stocum, *Amphibians as research models for regenerative medicine.* Organogenesis, 2010. 6(3): p. 141-50.

72. Rani, S.J.a.J.J., *Influence of natural long fiber in mechanical, thermal and recycling properties of thermoplastic composites in automotive components.* International Journal of Physical Sciences, 2012. 7(43): p. 5765-5771.

73. Truckenmüller, F. and H.G. Fritz, *Injection molding of long fiber-reinforced thermoplastics: A comparison of extruded and pultruded materials with direct addition of roving strands.* Polymer Engineering & Science, 1991. 31(18): p. 1316-1329.

74. Stokes, V.K., et al., *A phenomenological study of the mechanical properties of long-fiber filled injection-molded thermoplastic composites.* Polymer Composites, 2000. 21(5): p. 696-710.

75. Nguyen, B.N., et al., *Fiber Length and Orientation in Long-Fiber Injection-Molded Thermoplastics -- Part I: Modeling of Microstructure and Elastic Properties.* Journal of Composite Materials, 2008. 42(10): p. 1003-1029.

76. Lundberg, R., et al., *Effects of short-term exposure to the DDT metabolite p,p'-DDE on bone tissue in male common frog (Rana temporaria).* J Toxicol Environ Health A, 2007. 70(7): p. 614-9.

77. Shaw, S.D., et al., *Fluorosis as a probable factor in metabolic bone disease in captive New Zealand native frogs (Leiopelma species).* J Zoo Wildl Med, 2012. 43(3): p. 549-65.

78. Bernasconi, A., F. Cosmi, and P.J. Hine, *Analysis of fibre orientation distribution in short fibre reinforced polymers: A comparison between optical and tomographic methods.* Composites Science and Technology, 2012. 72(16): p. 2002-2008.

79. Krenkel, W., *Ceramic matrix composites : fiber reinforced ceramics and their applications*2008, Weinheim: Wiley-VCH. xxi, 418 p.

80. Cosmi, F., A. Bernasconi, and N. Sodini, *Phase contrast micro-tomography and morphological analysis of a short carbon fibre reinforced polyamide.* Composites Science and Technology, 2011. 71(1): p. 23-30.

Table and Figures

Table 1 Parameters measured by AMIRA software

Parameter	Definition	Unit
Porosity	The ratio of the volume of voids to the volume of the total volume	%
Area3D	The area of the object boundary	μm^2
Euler characteristic	An indicator of the connectedness of a 3D complex structure	N/A
Fractal dimension	An indicator to measure and compare the roughness of a surface	N/A
Orientation	The angle between the orientation, second orientation of the particle and the Z axis	Degree
Fragmentation	The indicator of connectivity	N/A
Thickness	The thickness of the structure for a 3d image	μm

Table 2 Groups assigned by freezing period

Group name	Freezing period	Harvest date	Number of samples
Group A	5 years	2008	20
Group B	1 year	5/15/2012	23
Group C	0 (not frozen)	5/30/2013	24

Table 3 One way ANOVA test results for each group

	Normality Test(p values)		Variance(p values)	Mean(p values)
Modulus	Group A	0.51061	0.73551	0.000009
	Group B	0.35491		
	Group C	0.76096		
Strength	Group A	0.20253	0.69159	0.00434
	Group B	0.05704		
	Group C	0.243		

Table 4 Correlation coefficients for each parameter

	Modulus			Strength		
	Group A	Group B	Group C	Group A	Group B	Group C
Porosity	-0.10	-0.17	-0.64	-0.59	-0.65	-0.88
Thickness	0.12	0.07	0.50	0.60	0.65	0.75
Apparent density	0.17	0.22	0.70	0.70	0.65	0.85
Density	0.30	-0.01	-0.10	0.17	0.13	-0.26
Mineral content	-0.18	-0.34	-0.16	-0.32	-0.39	-0.35
Fractal dimension	0.26	0.37	0.42	0.35	0.44	0.36
Fragmentation	-0.20	-0.23	-0.65	-0.49	-0.52	-0.69
Area3D	0.34	0.41	0.32	0.30	0.37	0.17
Euler characteristic	0.08	-0.17	-0.28	0.17	0.00	-0.21
Orientation	0.18	-0.33	-0.01	0.31	-0.39	-0.07
Orientation2	-0.14	0.39	0.23	-0.26	0.49	0.22

Table 5 Value of parameters considered for the multiple regression

Parameter		**Group A**	**Group B**	**Group C**
Porosity(%)	Mean	7.06E+01	6.59E+01	6.86E+01
	SD	5.06E+00	4.85E+00	3.92E+00
Thickness (μm)	Mean	1.96E+02	2.21E+02	2.03E+02
	SD	2.69E+01	2.40E+01	1.86E+01
Apparent Density (g/mm^3)	Mean	6.72E-04	8.05E-04	7.42E-04
	SD	1.40E-04	1.47E-04	9.13E-05
Density (g/mm^3)	Mean	2.27E-03	2.36E-03	2.37E-03
	SD	1.80E-04	2.18E-04	1.31E-04
Mineral content (mg/cm^3)	Mean	1.18E+03	1.13E+03	1.19E+03
	SD	8.97E+01	6.39E+01	8.49E+01
Fractal dimension	Mean	2.42E+00	2.46E+00	2.48E+00
	SD	4.01E-02	2.44E-02	2.20E-02
Fragmentation	Mean	-1.75E-03	-4.17E-03	-4.23E-03
	SD	2.38E-03	2.08E-03	1.39E-03
Area3D (μm^2)	Mean	7.59E+08	8.40E+08	1.02E+09
	SD	1.18E+08	8.25E+07	1.25E+08
Euler characteristic	Mean	-3.34E+03	-3.77E+03	-4.68E+03
	SD	1.45E+03	1.19E+03	8.55E+02
Orientation(degree)	Mean	2.79E+01	2.31E+01	1.93E+01
	SD	2.45E+01	1.67E+01	3.77E+00
Orientation2(degree)	Mean	6.66E+01	7.73E+01	8.81E+01
	SD	2.59E+01	2.12E+01	1.51E+00

Table 6 Linear coefficients for each parameter

Parameter	Group A	Group B	Group C
Intercept	205.7337	61.29279	-813.551
Porosity	-2.68766	0.815935	3.947676
Thickness	-0.0845	-0.05841	0.114654
Apparent density	-121500	47646.29	195669.9
Density	42529.06	-12457.1	-57696.1
Mineral content	0.001845	-0.00547	0.003719
Fractal dimension	-7.11521	-52.9535	239.6608
Fragmentation	-2046.93	-1377.49	953.4264
Area3D	1.07E-08	4.43E-08	1.3E-08
Euler characteristic	0.003832	0.004864	0.004234
Orientation	0.119628	0.130391	-0.47172
Orientation2	0.135945	0.14045	-0.60402

Table 7 Frog tarsus perimeter measurements

Slice	Astragalus (Pixels)	Calcaneum (Pixels)	Astragalus (μm)	Calcaneum (μm)
0	370	452	3370.7717	4145.1938
25	372	416	3187.417	3613.2749
50	359	380	2878.8752	3298.2712
75	305	352	2642.208	3071.1851
100	304	350	2589.7839	2982.792
125	294	338	2514.1138	2888.8535
150	294	364	2472.0522	2822.2432
175	275	332	2275.806	2784.3501
200	272	332	2235.007	2799.729
225	271	338	2250.886	2809.4116
250	300	340	2473.634	2830.9858
275	304	344	2591.0427	2869.75
300	316	354	2661.7476	2930.2722
325	326	358	2753.8113	3020.1069
350	340	374	2898.8679	3174.897
375	358	396	3036.241	3380.9299
400	376	414	3232.3376	3615.9192
425	392	438	3393.5781	3845.6807
450	426	480	3619.7961	4164.1367
475	450	506	3872.2256	4529.8345
500	474	530	4299.9048	4906.9575

Table 8 Frog tarsus mineral density

Position	**Slices**	**Calceneum (** mg/cm^3 **)**	**Astragalus (** mg/cm^3 **)**
Bottom	220-250	958.37	1020.86
Middle	350-450	1131.51	1058.78
Top	600-630	958.78	894.04

Table 9 Thermoplastic fiber orientaions

	Fiber numbers	**Average(degrees)**	**SD(degrees)**
Slice (0-3)	855	38.15	29.75
Slice (35-38)	812	25.64	28.15
Slice (70-73)	879	19.09	26.97
Slice (105-108)	946	23.76	27.78
Slice (140-143)	852	25.95	27.89
Slice (175-178)	635	29.48	26.9
Slice (210-213)	696	26.35	27.57
Slice (245-248)	619	28.98	26.1
Slice (280-283)	648	31.63	27.55
Slice (315-318)	763	36.76	26.34
Slice (350-353)	1976	51.85	32.12
Slice (385-388)	1976	46.96	31.03
Slice (420-423)	1976	41.05	35.07
Slice (455-458)	1976	39.18	33.31
Slice (490-493)	1976	36.62	33.3
Slice (525-528)	1976	36.35	34.81
Slice (560-563)	1976	34.93	35.44
Slice (595-598)	884	18.9	26.52
Slice (630-633)	884	21.86	27.85
Slice (665-668)	884	26.02	27.81

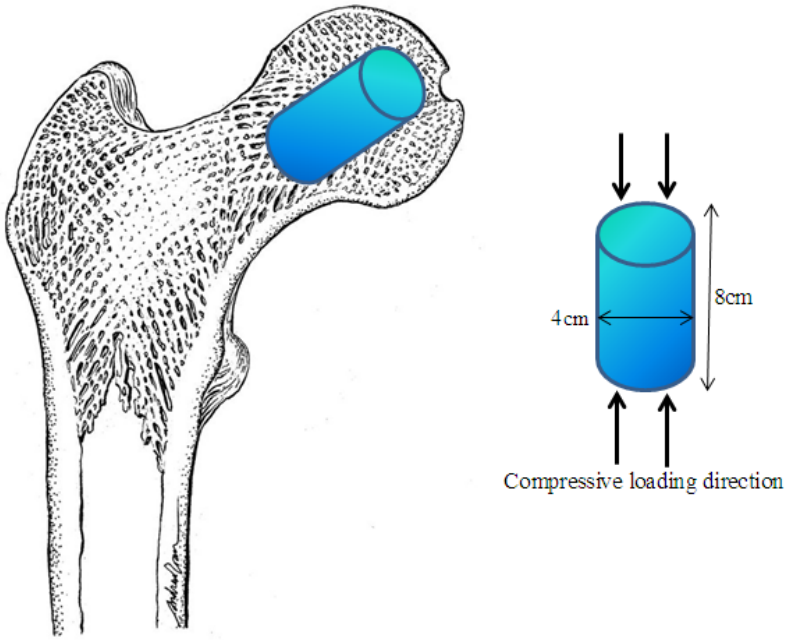

Figure 1 Cylindrical samples formed at longitudinal direction and compressive load applied to it

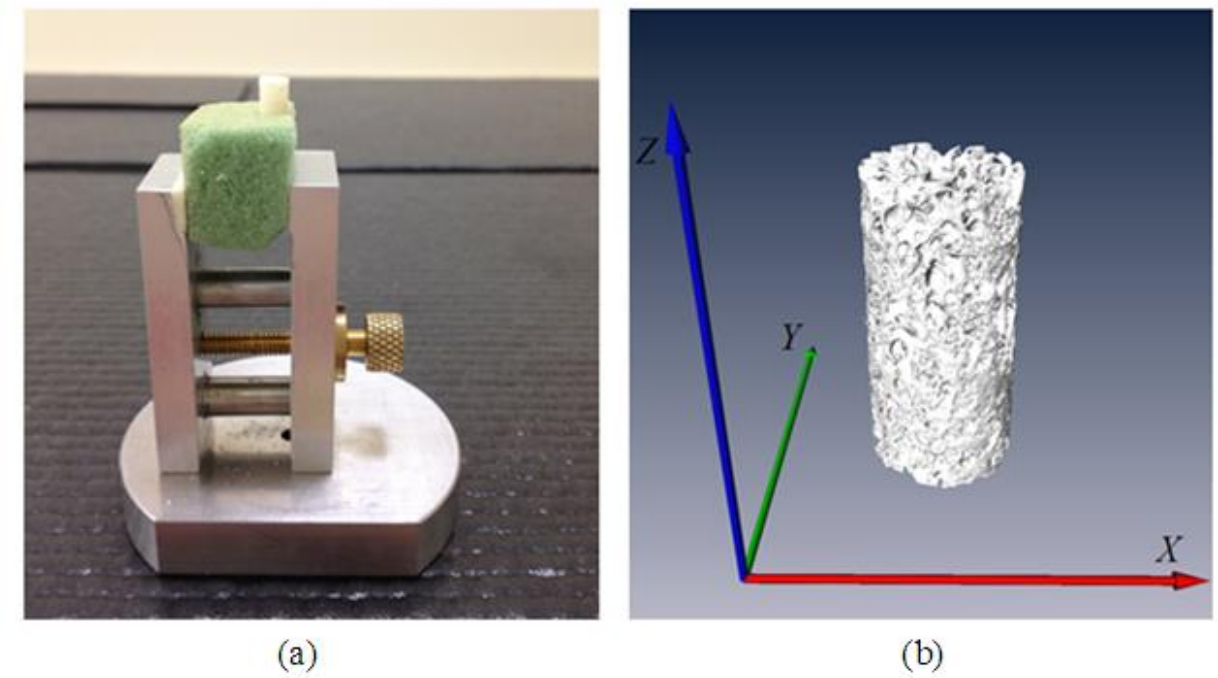

Figure 2 Trabecular bone sample (a) on the sample holder for micro-CT and (b) images post processed with AMIRA

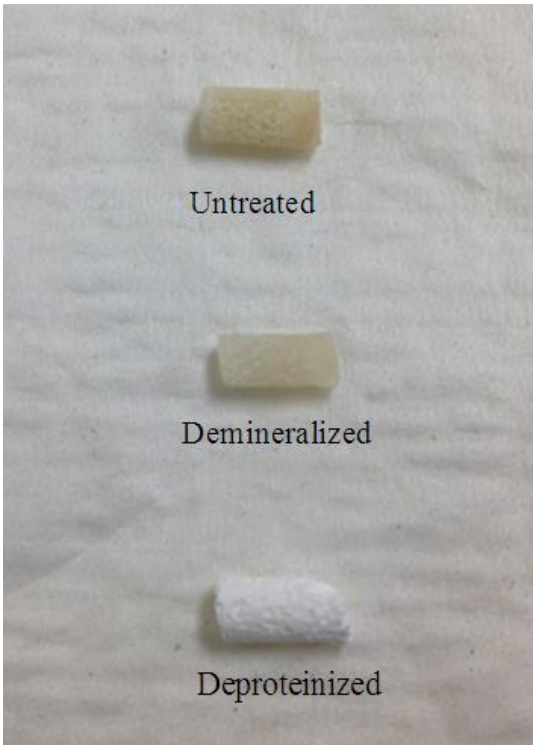

Figure 3 Chemically treated samples

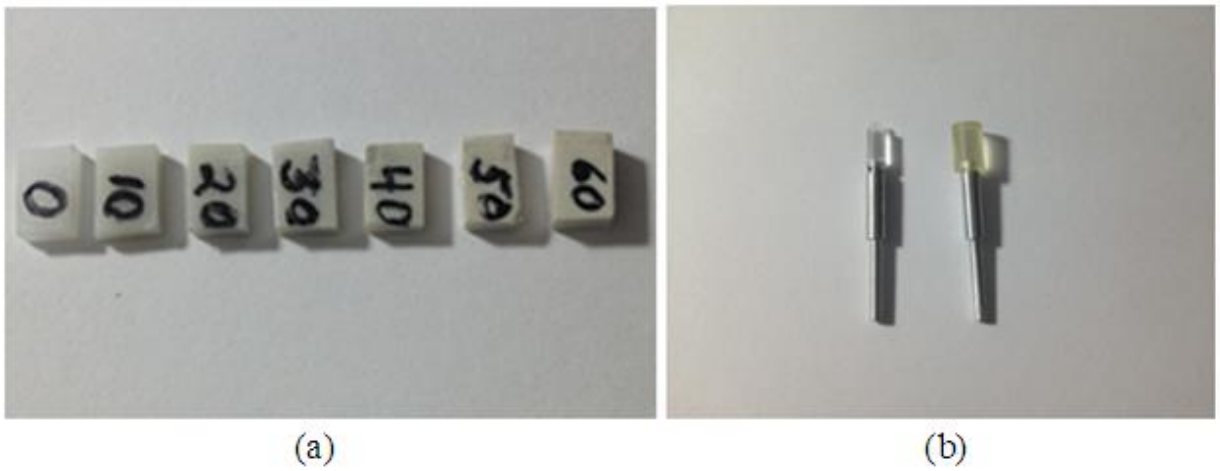

Figure 4 (a) HA phantoms, (b) Water Phantoms

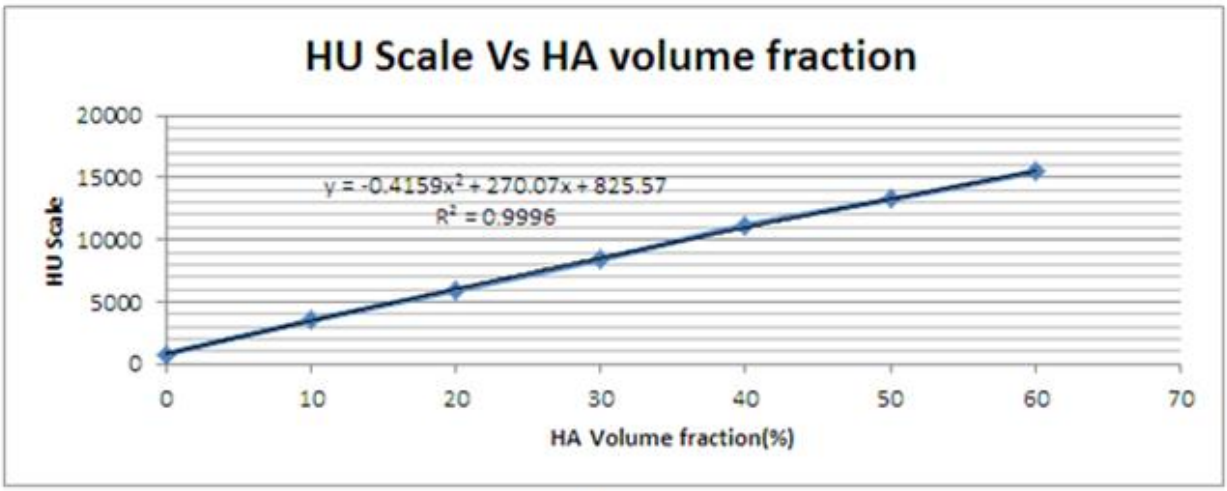

(a)

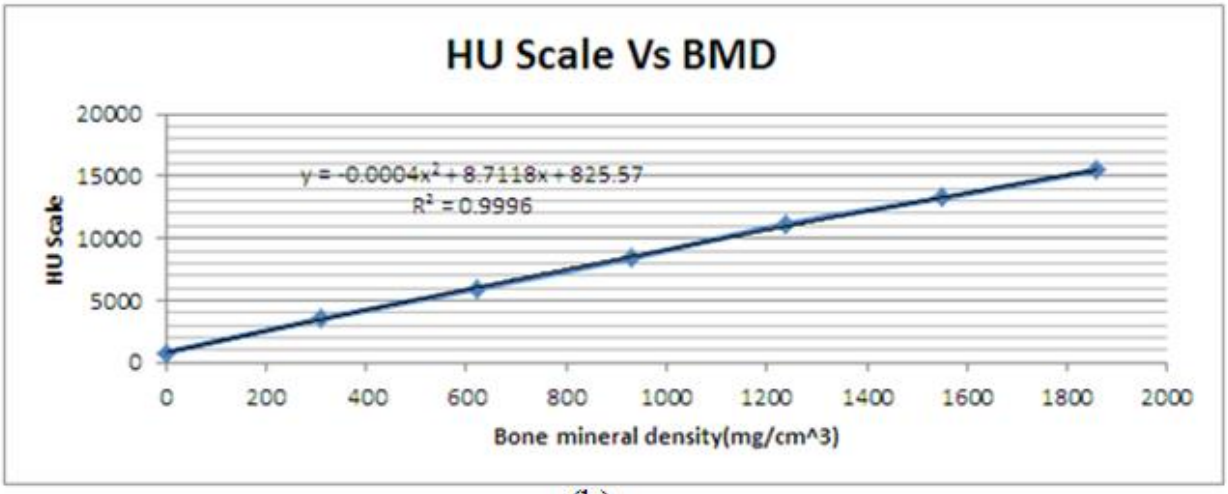

(b)

Figure 5 Quadratic curve for (a) HU scale verses HA volume fraction (b) HU scale verses bone mineral density

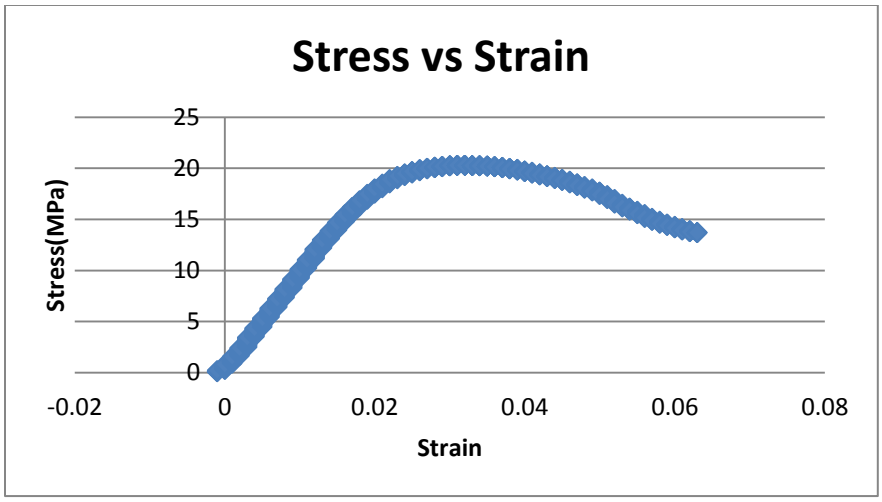

Figure 6 Stress verses strain curve for a porcine trabecular bone sample.

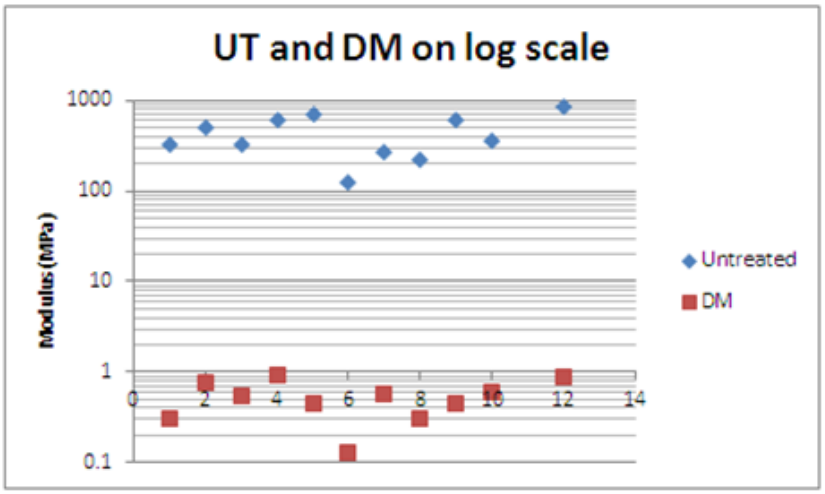

(a)

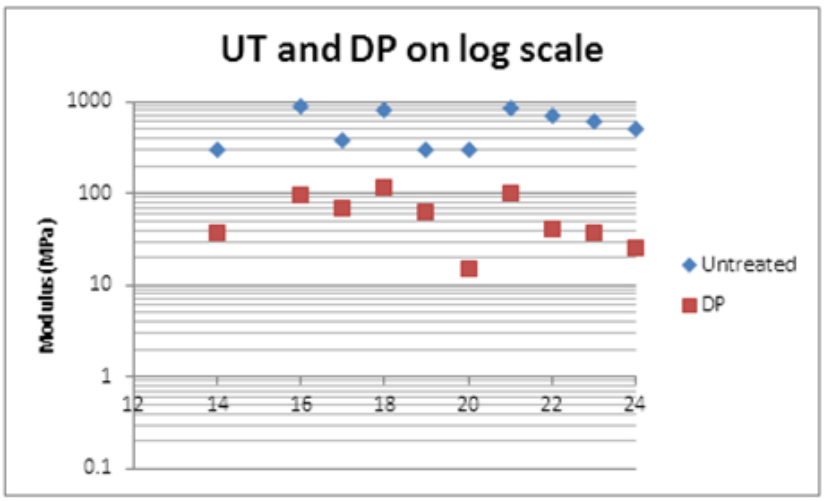

(b)

Figure 7 Comparison of the Young's modulus of (a) untreated and demineralized, (b) untreated and deproteinized samples

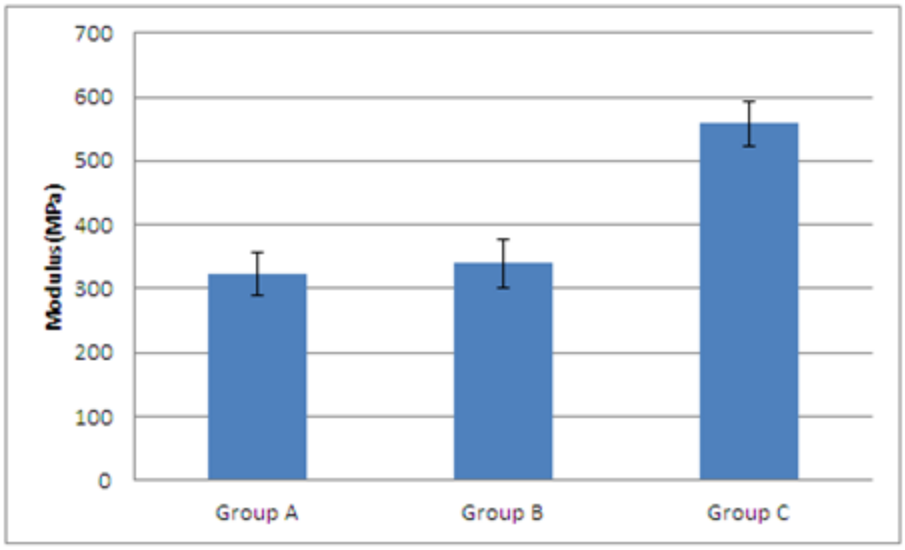

(a)

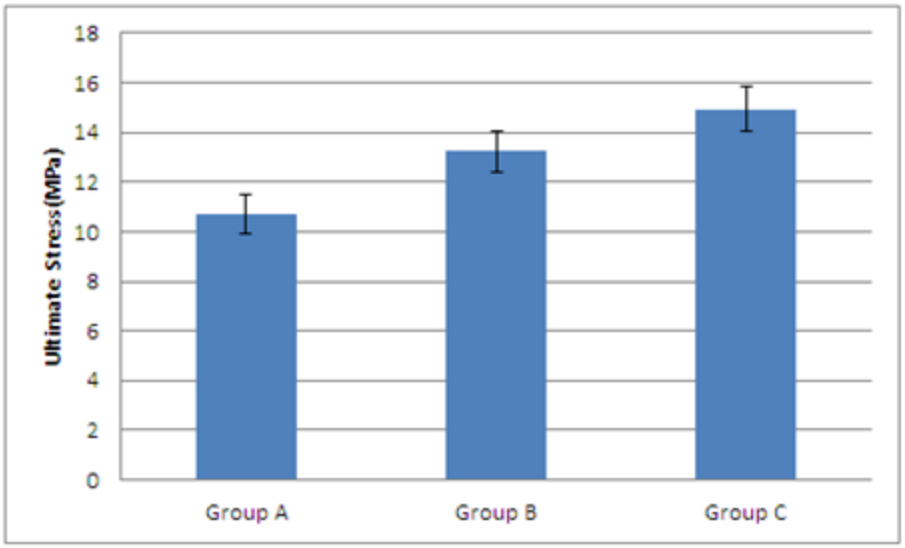

(b)

Figure 8 Average (a) Young's modulus, (b) ultimate stress of group A, B and C

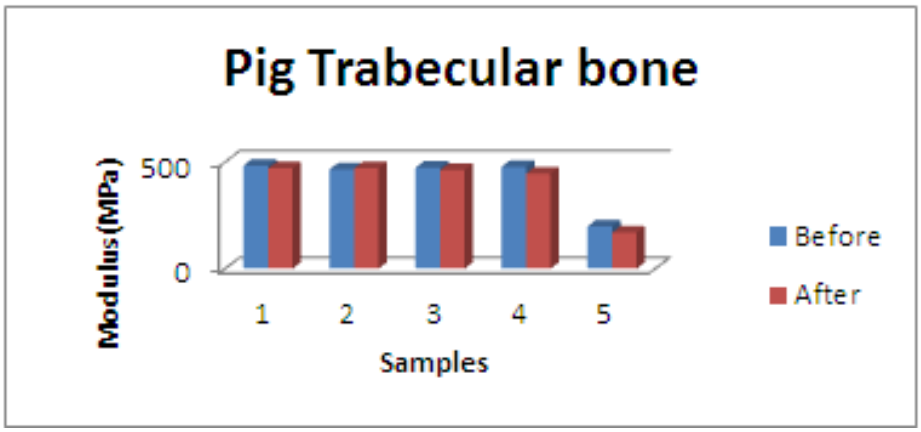

Figure 9 Comparison of Young's modulus before and after X-ray irradiation

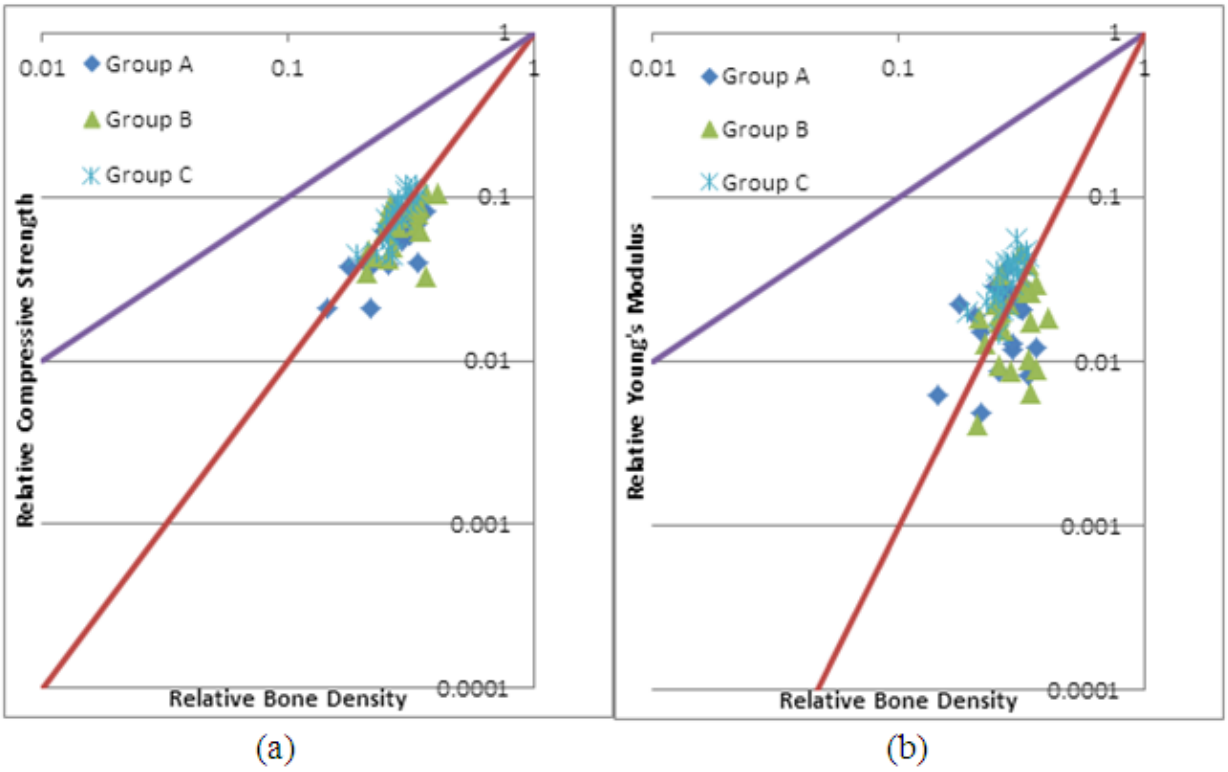

Figure 10 (a) Compressive strength plotted against density. Compressive strength is normalized by 190 MPa (b) Young's moduli plotted against density. Young's modulus is normalized by 17GPa. Apparent density is normalized by 2505.58, 2732.40, 2685.87 kg/m^3 respectively for group A, B and C

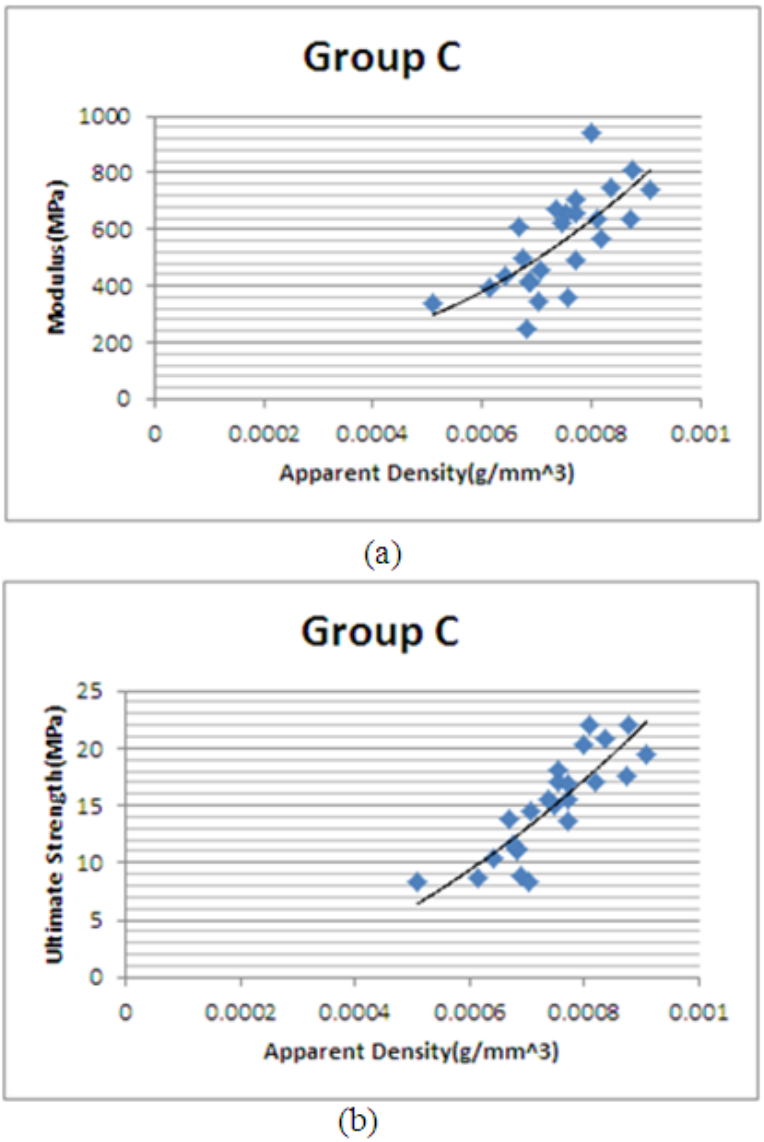

Figure 11 Fresh porcine bone quadratic fit between (a) Young's modulus and apparent density, (b) Ultimate strength and apparent density

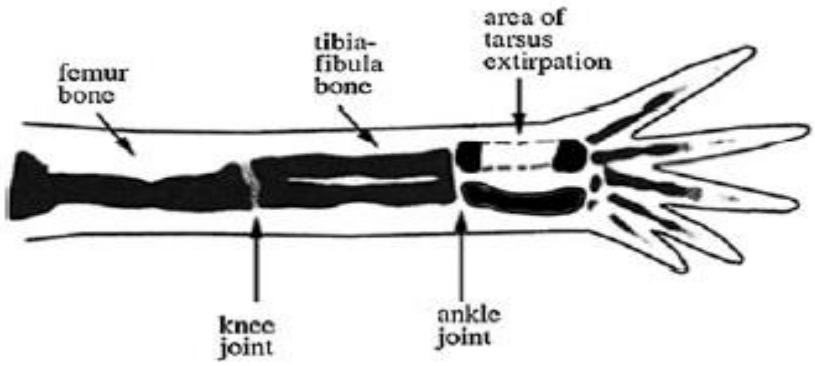

Figure 12 Frog tarsus bone extirpation

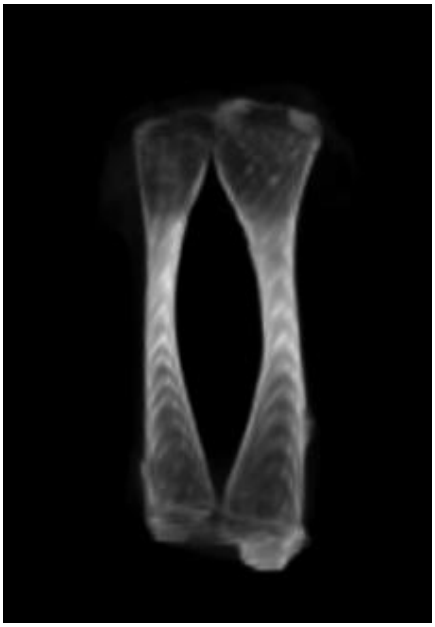

Figure 13 3-D images of frog tarsus bone generated by CTan

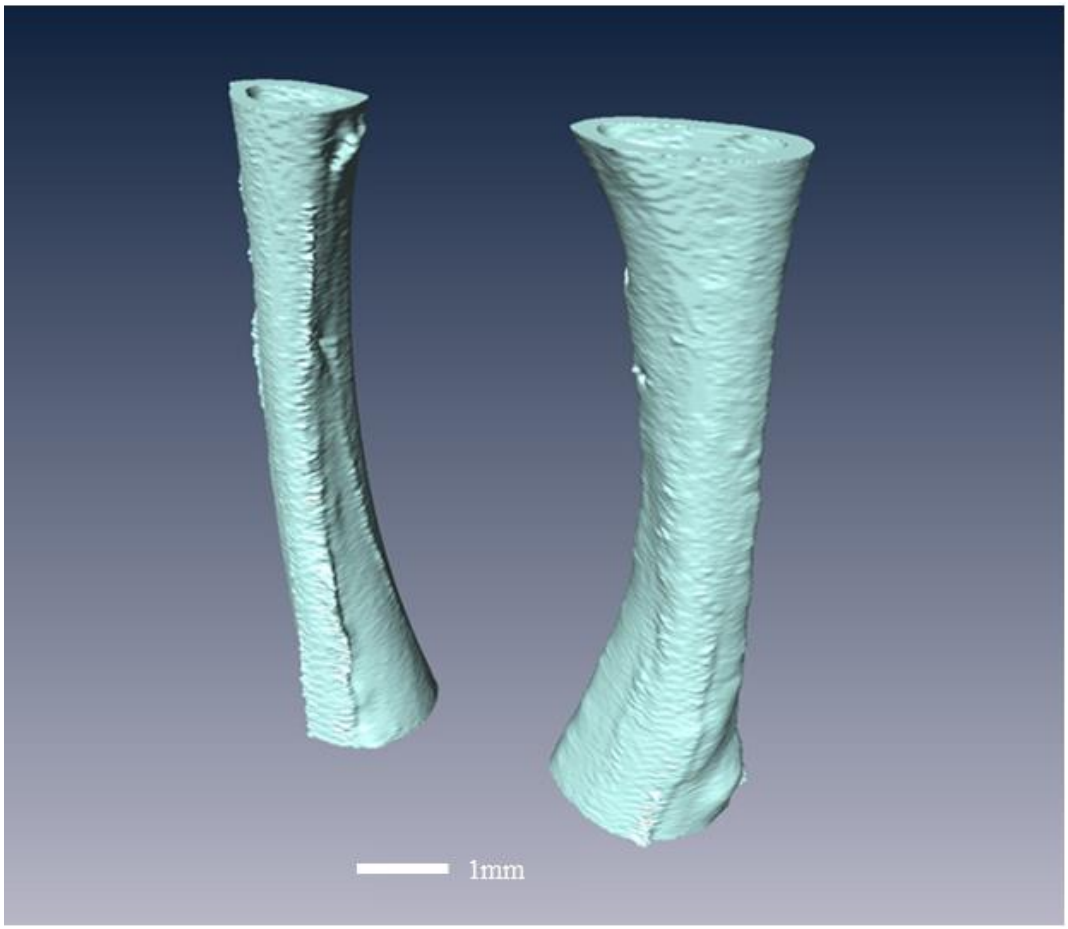

Figure 14 3-D images of frog tarsus bone middle section generated by AMIRA

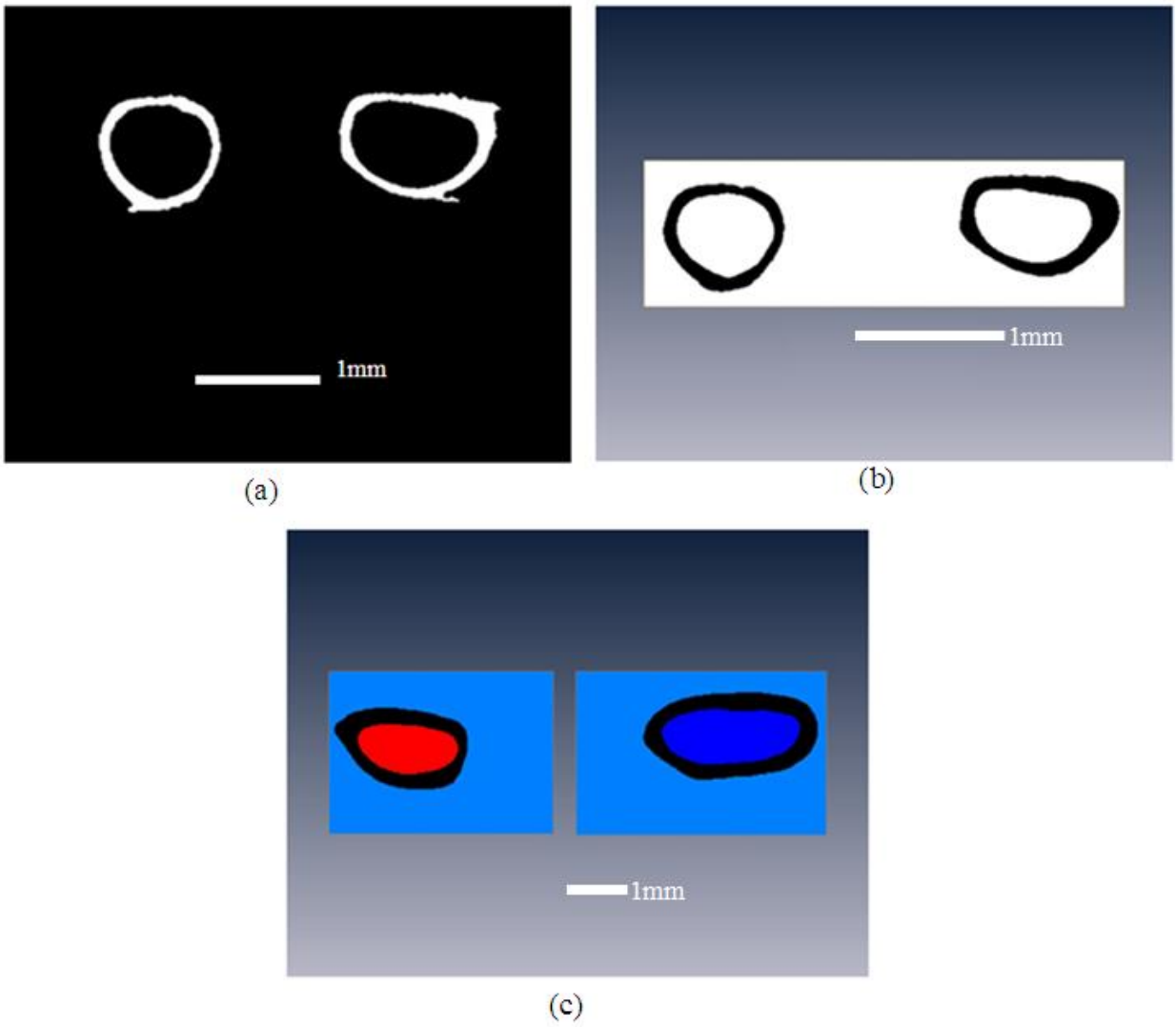

Figure 15 Cross section of frog tarsus bone (a) binarized (b) inversed and (c) separated using brush tool

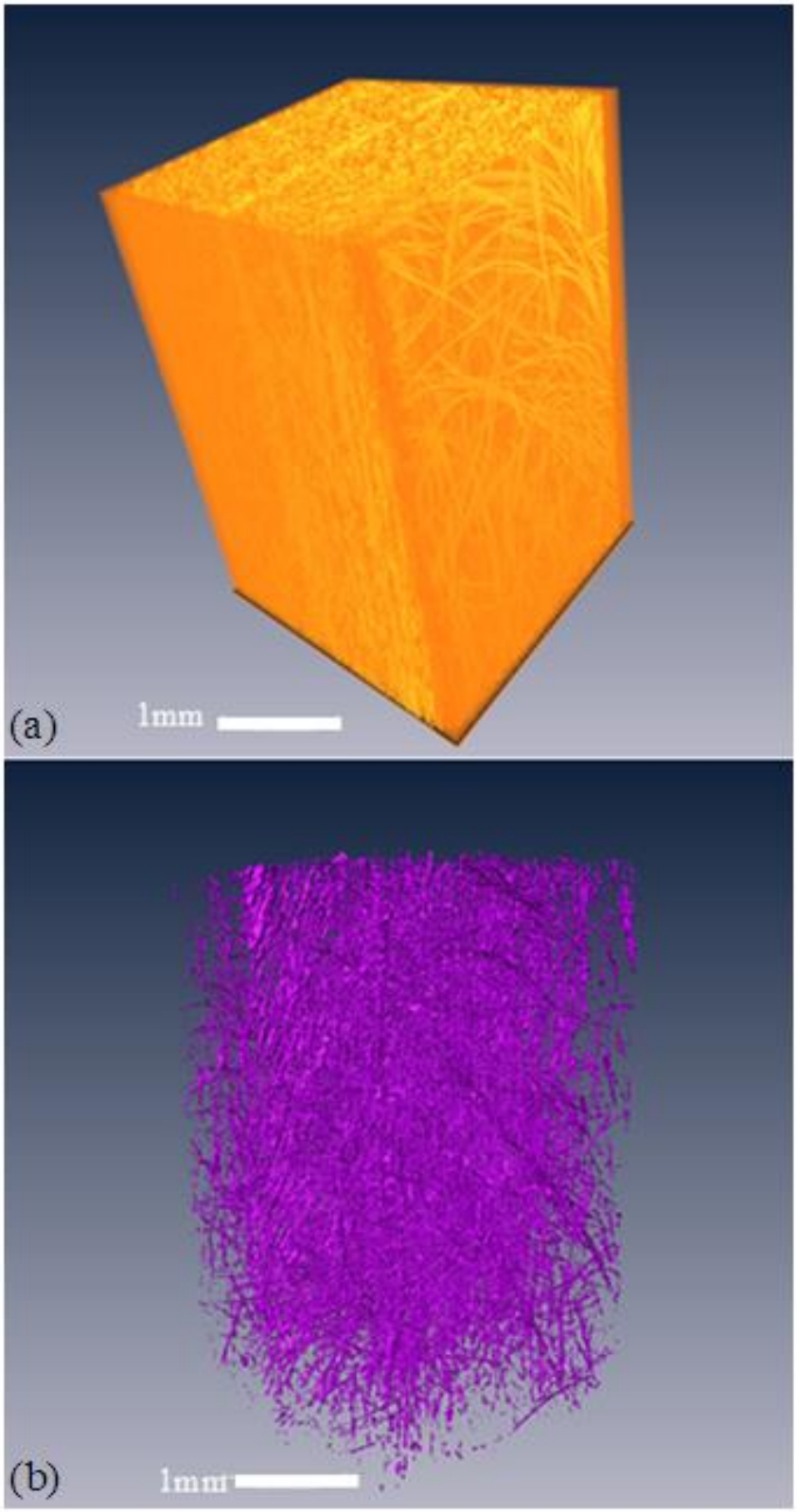

Figure 16 3-D images of (a) thermoplastic (b) the fibers solely

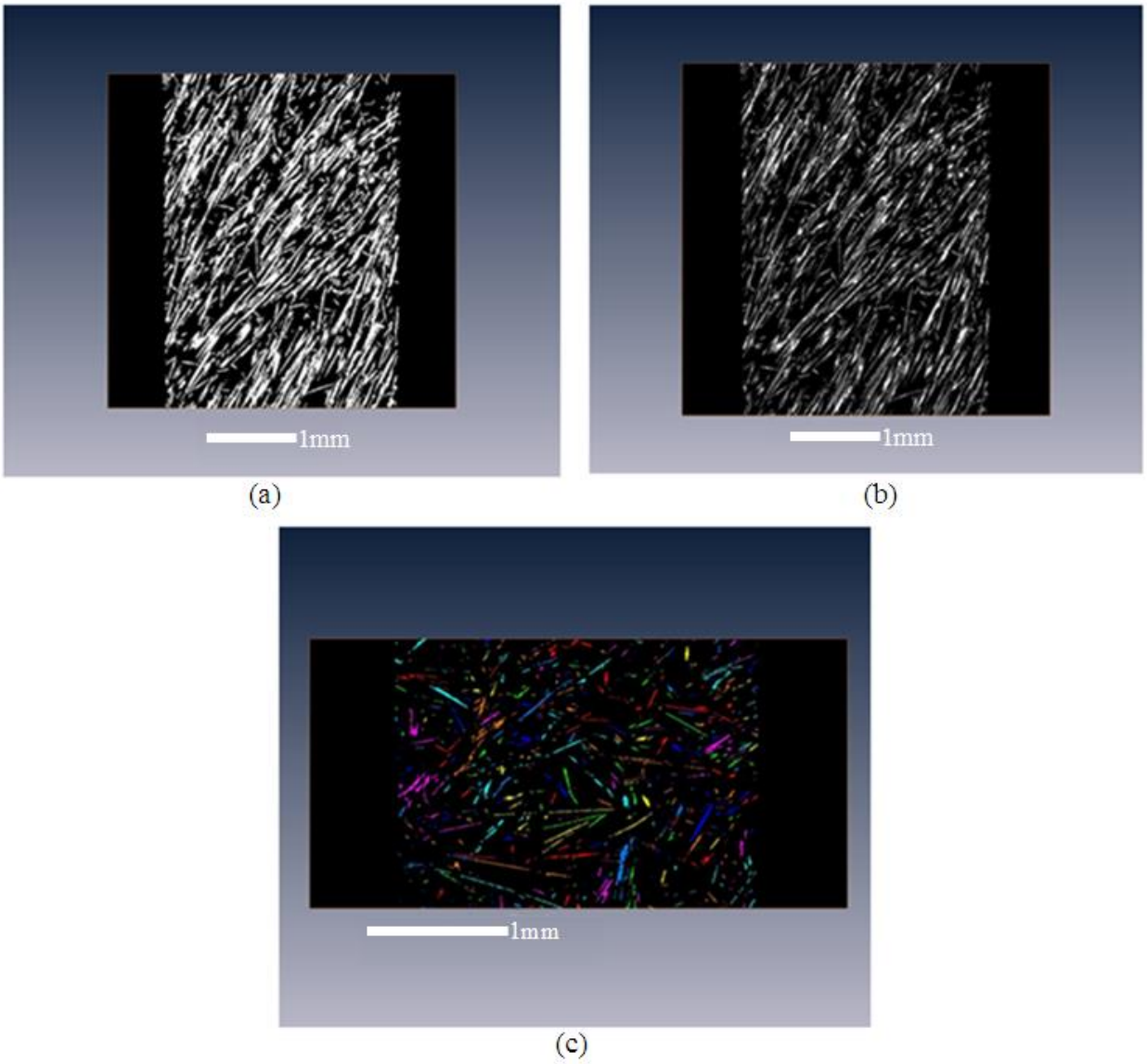

Figure 17 Cross sections of thermoplastic for the (a) initial binarized image (b) after applying Distance map module (c) Orientation command in Quantification

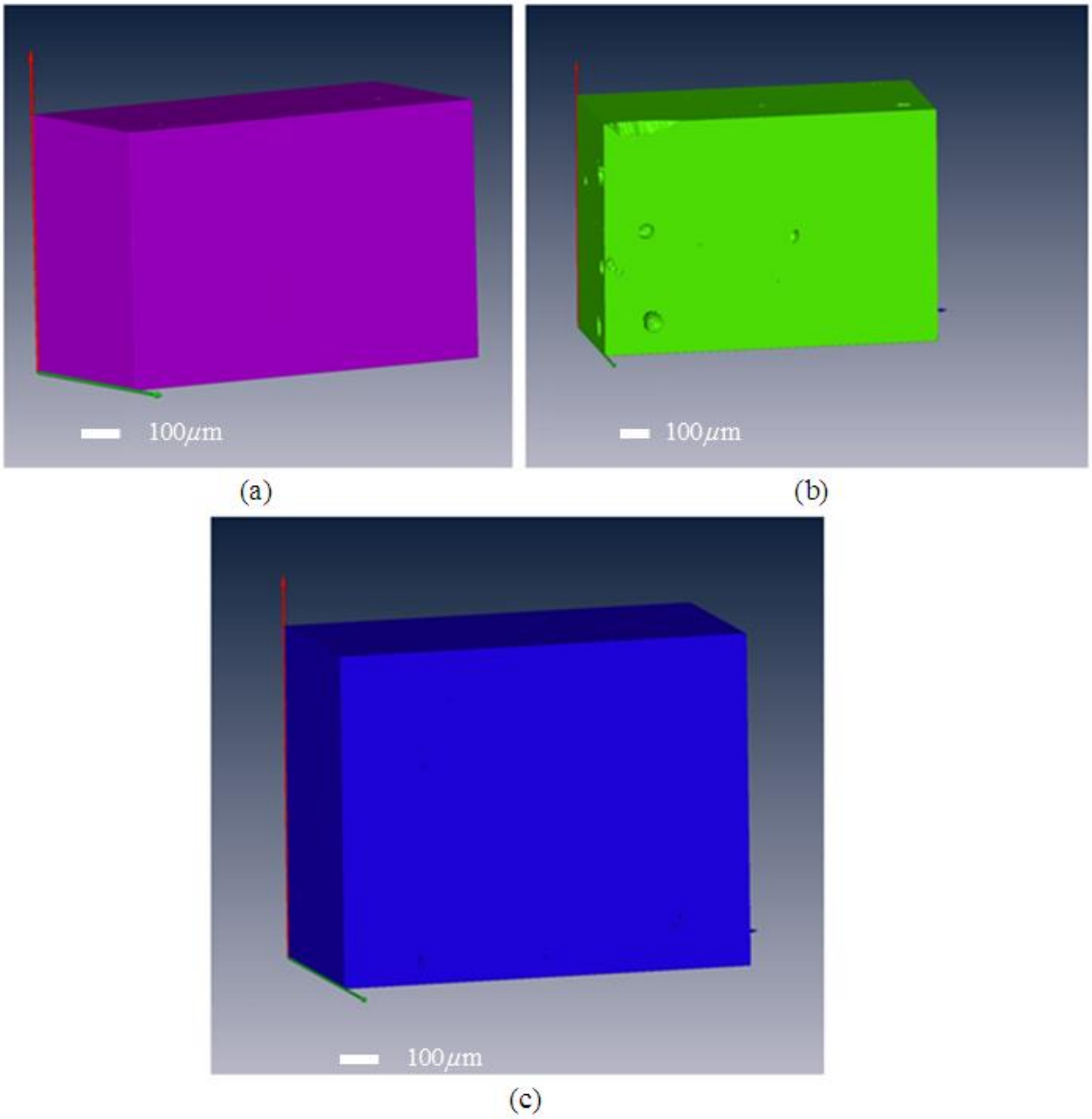

Figure 18 3-D images of 7075 Al covetics with (a) 0% (b) 3% and (c) 5% wt carbon

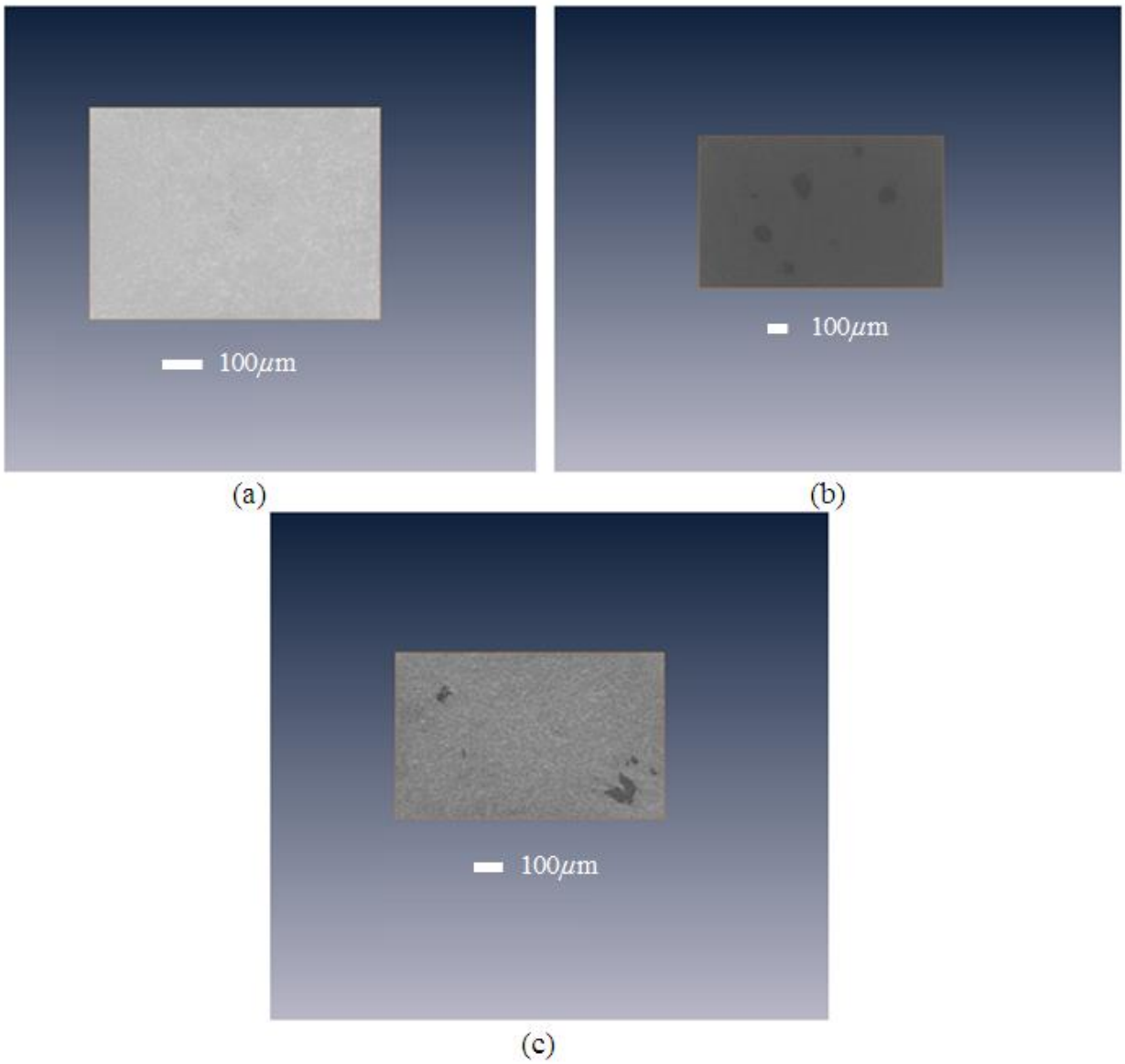

Figure 19 Cross sections of 7075 Al covetics with (a) 0% (b) 3% and (c) 5% wt carbon

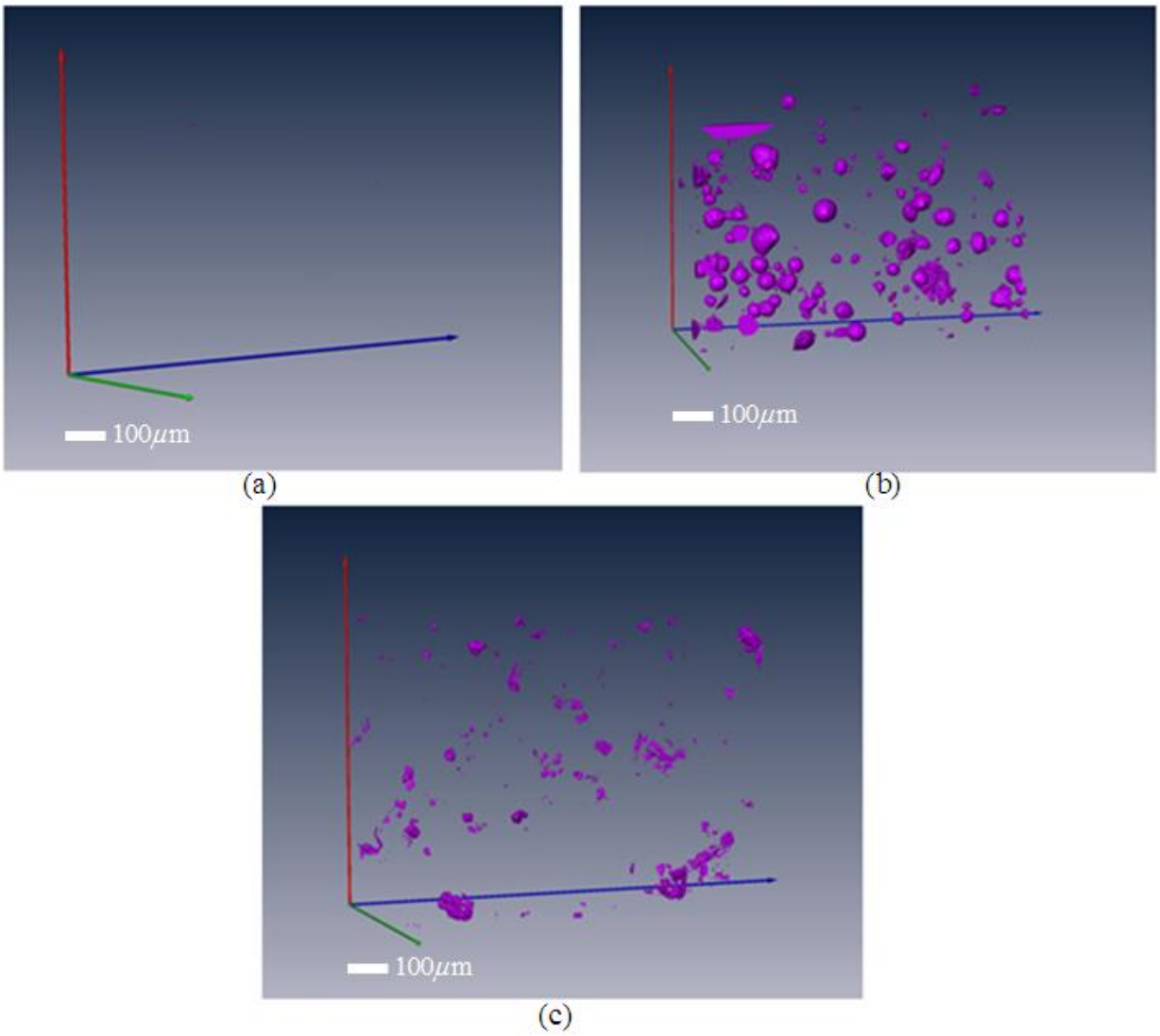

Figure 20 3-D images of 7075 Al covetics pores with (a) 0% (b) 3% and (c) 5% wt carbon